

# 9

## Seismic Arrays

Johannes Schweitzer, Jan Fyen, Svein Mykkeltveit  
and Tormod Kværna

### 9.1 Outline

When Willmore (1979) published his Manual of Seismological Observatory Practice, only a small number of seismic arrays were in operation. The whole section on array seismology in that issue of the Manual was no longer than two pages, including one figure; array seismology being at that time more a matter of some specialists rather than a commonly applied technique. During the last two decades, new seismic arrays were installed all over the globe and, due to digital data acquisition systems and digital signal processing, it has become easier to handle the large amount of data from seismic arrays. Therefore, array observations have become more commonly used. This requires a separate Chapter on array seismology in the New Manual of Seismological Observatory Practice, which explains the principles of seismic arrays and how their data can be used to analyze seismic observations.

In the following sections we define first the term “seismic array” and show examples of seismic arrays installed around the world. We then describe the theoretical basics of the processing of seismic data observed with an array, continue with the explanation of helpful tools for automatic analysis of array data and explain how local and regional events are located at the NORSAR Data Processing Center by using single array observations. Finally, we describe some helpful rules and procedures to find the best configuration for a seismic array and present a table of operational and planned seismic arrays.

### 9.2 Introduction

“The Conference of Experts to study the methods of detecting violations of a possible agreement on the suspension of nuclear tests” held in 1958 in Geneva under the auspices of the United Nations, was followed by several initiatives for improving the quality of seismic stations worldwide. At the same time, the idea of installing arrays of sensors to improve the signal-to-noise ratio was adopted from radio astronomy, radar, acoustics, and sonar. In the 1960s, it was demonstrated that seismic arrays are superior to single three-component stations for detecting and characterizing signals from earthquakes and explosions. A seismic array differs from a local network of seismic stations mainly by the techniques used for data analysis. Thus, in principle, a network of seismic stations can be used as an array, and data from an array can be analyzed as from a network. However, most array processing techniques require high signal coherency across the array, and this puts important constraints on the array geometry, spatial extent, and data quality. Furthermore, proper analysis of array data is

## 9. Seismic Arrays

dependent on a stable, high precision relative timing of all array elements. This is required because the measurement of (usually very small) time differences of the arrival of seismic signals between the different sensors plays an important role in all array-processing techniques.

The superior signal detection capability of arrays is obtained by applying “beamforming” techniques, which suppress the noise while preserving the signal, thus enhancing the signal-to-noise ratio (SNR).

Arrays can also provide estimates of the station-to-event azimuth (backazimuth), and of the apparent velocity of different types of signals. These estimates are important both for event location purposes and for classification of signals, e.g., P, S, local, regional, or teleseismic.

In this chapter we describe procedures for estimating the apparent wavefront velocity (inverse of the slowness or ray parameter), the angles of approach (backazimuth and incidence angle) of a seismic signal as well as basic processing algorithms for signal detection, one-array regional phase association, and the preparation of an automatic event bulletin.

At the NORSAR Data Processing Center (NDPC) at Kjeller, Norway, data have been acquired for many years from different types of arrays: e.g., the large aperture NORSAR array, the small aperture arrays NORES and ARCES and the very small aperture arrays at Spitsbergen and in Apatity, Kola peninsula. The processing algorithms for a large array are different from the processing techniques used for the smaller arrays. The processing techniques for both types of arrays are described below.

We aim also at describing the general array processing techniques for training purposes and for use as a reference for analysts new to the field of seismic array processing. Some algorithms are described in detail, whereas others have references to available literature. It is assumed that the reader has basic knowledge about time-series analysis like bandpass filtering and Fourier transforms (e.g., Scherbaum, 2001).

The amount of data arising from use of an array of seismometers and digital signal processing techniques is enormous. Low-threshold detection processing leads to numerous triggers, which have to be analyzed. It is therefore of great importance to use techniques that are robust and easy to operate in an automatic, uninterrupted mode. The automatic processing steps used at NDPC are divided into three separate cases:

- Detection Processing (DP), which uses beamforming, filtering and STA/LTA detectors to define signal triggers;
- Signal Attribute Processing (SAP), which uses techniques like frequency-wavenumber (f-k) analysis to estimate the slowness vector, and other techniques to estimate parameters like onset time, period, amplitude and polarization attributes for every trigger; and
- Event Processing (EP), which analyzes the attributes and sequence of triggers to associate seismic phase arrivals to define events.

In Mykkeltveit and Bungum (1984), documentation of this method can be found with results from the first program (called RONAPP) for detecting and associating seismic signals from regional events using data from the regional array NORES.

Later, the automatic processing was re-coded to adapt to any array, several data formats and machine architectures. The programs are packaged into DP for continuous detection processing, and EP for automatic signal attribute processing, event processing, and interactive special processing (Fyen, 1989, 2001). These programs have been used for all examples herein. Section 9.8.2 shows the output of this automatic data processing for some signals observed on the ARCES array as an example of routine data analysis.

It is difficult to find publications that give details about basic array processing. There are numerous papers about advanced techniques and results from observations, but the basics of beamforming and STA/LTA detection processing are mostly assumed to be known. The type of processing used is similar to what is done in many types of signal-processing applications and time-series analysis. The algorithms are used in radar technology and in seismic prospecting. In seismic prospecting “beamforming” is called “stacking”.

The first large seismic array, LASA, was built in Montana, USA, in the mid-1960s (Frosch and Green, 1966). The *Seismic Array Design Handbook*, August 1972 by IBM, describes the processing algorithms for LASA and NORSAR. References therein are mostly to reports prepared by J. Capon and R. T. Lacoss, Lincoln Laboratories. These basic processing techniques developed in the 1960s have survived, and are still in use.

The description for many array methods and early array installations can be found in a proceeding volume (Beauchamp, 1975) of a NATO Advanced Study Institute conference in 1974 in Sandefjord, Norway. Also several NORSAR Scientific Reports describe array-processing techniques. For example, Kværna and Doornbos (1986) report on f-k analysis techniques using the integration over a wider frequency band (so-called “broadband f-k analysis”) rather than the single frequency-wavenumber analysis (e.g., Capon, 1969) as applied by many authors.

In 1990, a special issue of the *Bulletin of the Seismological Society of America* was published (Volume **80**, Number 6B) with contributions from a symposium entitled “Regional Seismic Arrays and Nuclear Test Ban Verification”. This issue contains many papers on theoretical and applied array seismology. A more recent review on array applications in seismology can be found in Douglas (2002) and in Rost and Thomas (2002).

## 9.3 Examples of seismic arrays

Throughout the text, we use examples from the processing of data from the large array NORSAR in southern Norway, from the “regional” arrays NORES in southern Norway and ARCES in northern Norway, and from the GERES array in southern Germany.

Fig. 9.1 shows the configuration of the ARCES array and Fig. 9.2 shows the layout of the seismometer sites for the NORSAR and NORES arrays. The NORES and ARCES-type array design of sites located on concentric rings (each consists of an odd number of sites) spaced at log-periodic intervals is now used for most of the modern small aperture arrays; only the number of rings and the aperture differ from installation to installation. The Spitsbergen array has only nine sites, e.g., and corresponds to the center site plus the A and the B rings of a NORES-type array; the FINES array consists of three rings with 15 sites altogether. These regional, relatively small arrays have been developed in the last 10 to 20 years.

## 9. Seismic Arrays

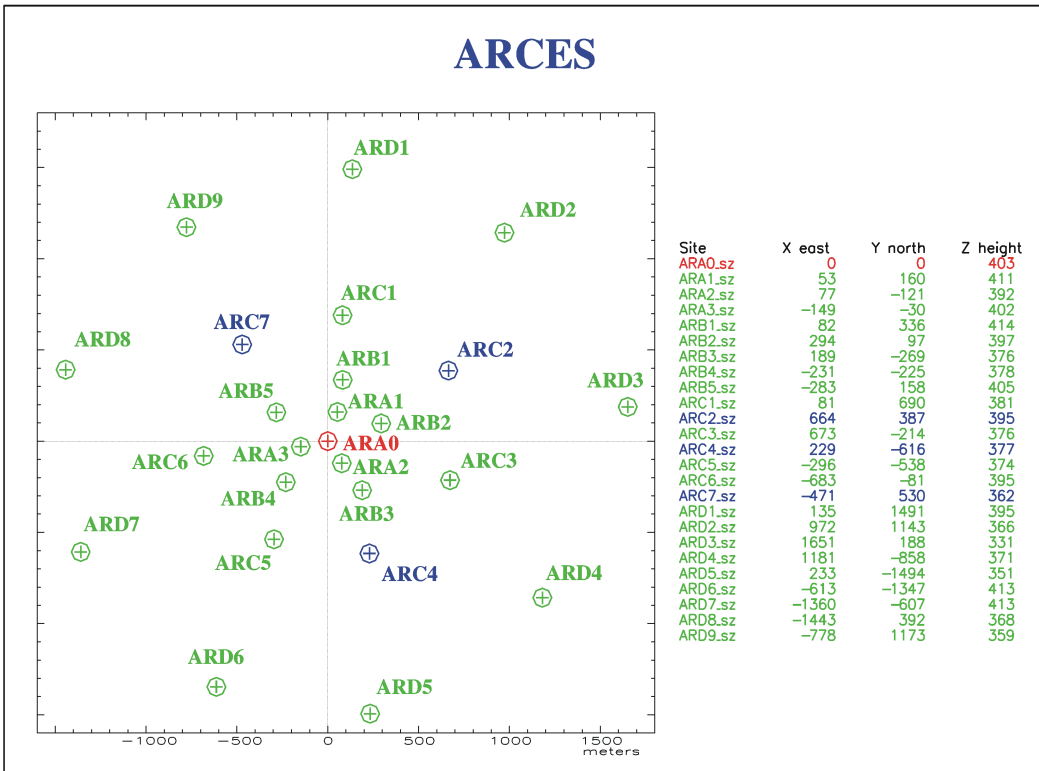


**Fig. 9.1** Configuration of the regional array ARCES, which is identical to the NORES array. Each vertical seismometer site is marked with a circle and a cross. The ARCES array has 25 sites with vertical seismometers. Four of these sites have in addition short-period horizontal seismometers. The short-period three-component sites are marked in blue or red. At the center site (red) a broadband three-component seismometer is collocated. The array has one center instrument – ARA0 – and four rings: the A-ring with three sites and a radius of about 150 m, the B-ring with five sites and a radius of about 325 m, the C-ring with seven sites and a radius of about 700 m, and finally, the D-ring with nine sites and a radius of about 1500 m. The center seismometer of ARCES has the geographic coordinates 69.53486°N, 25.50578°E. The table gives the relative coordinates between the single sites and the center site ARA0, and the elevation of all sites above sea level in meters.

To our knowledge, the first experimental seismic array with more than four elements was established in February 1961 by the United Kingdom Atomic Energy Agency (UKAEA) on Salisbury Plain (UK), followed in December 1961 by Pole Mountain (PMA, Wyoming, USA), in June 1962 by Eskdalemuir (EKA, Scotland, UK), and in December 1963 by Yellowknife (YKA, Canada), all with openly available data. These types of arrays (the so-called UK-arrays) are orthogonal linear or L-shaped. Later, arrays of the same type were built in Australia (Warramunga), Brasilia, and India (Gauribidanur). A detailed description of this type of arrays can be found in Keen et al. (1965), Birtill and Whiteway (1965), and Whiteway (1965, 1966). Fig. 9.3 shows the configuration of the Yellowknife array (Somers and Manchee, 1966, Manchee & Weichert, 1968, Weichert, 1975) as one example of this kind of medium-sized array, which is still in operation. The size of an array is defined by its aperture given by the largest (horizontal) distance between the single sensors. The apertures of the UKAEA arrays vary between 10 and 25 km.

In the 1960s, arrays were tested with very different aperture and geometry, from small circular arrays with apertures of some kilometers to huge arrays with apertures of up to 200 km. The largest arrays were the LASA array in Montana (USA), dedicated in 1965, with 525 seismometer sites (Frosch and Green, 1966) and the original NORSAR array in southern Norway consisting of 132 sites over an aperture of approximately 100 km with altogether 198 seismometers, which became fully operational in the spring of 1971 (Bungum et al., 1971).

## NORSAR and NORES

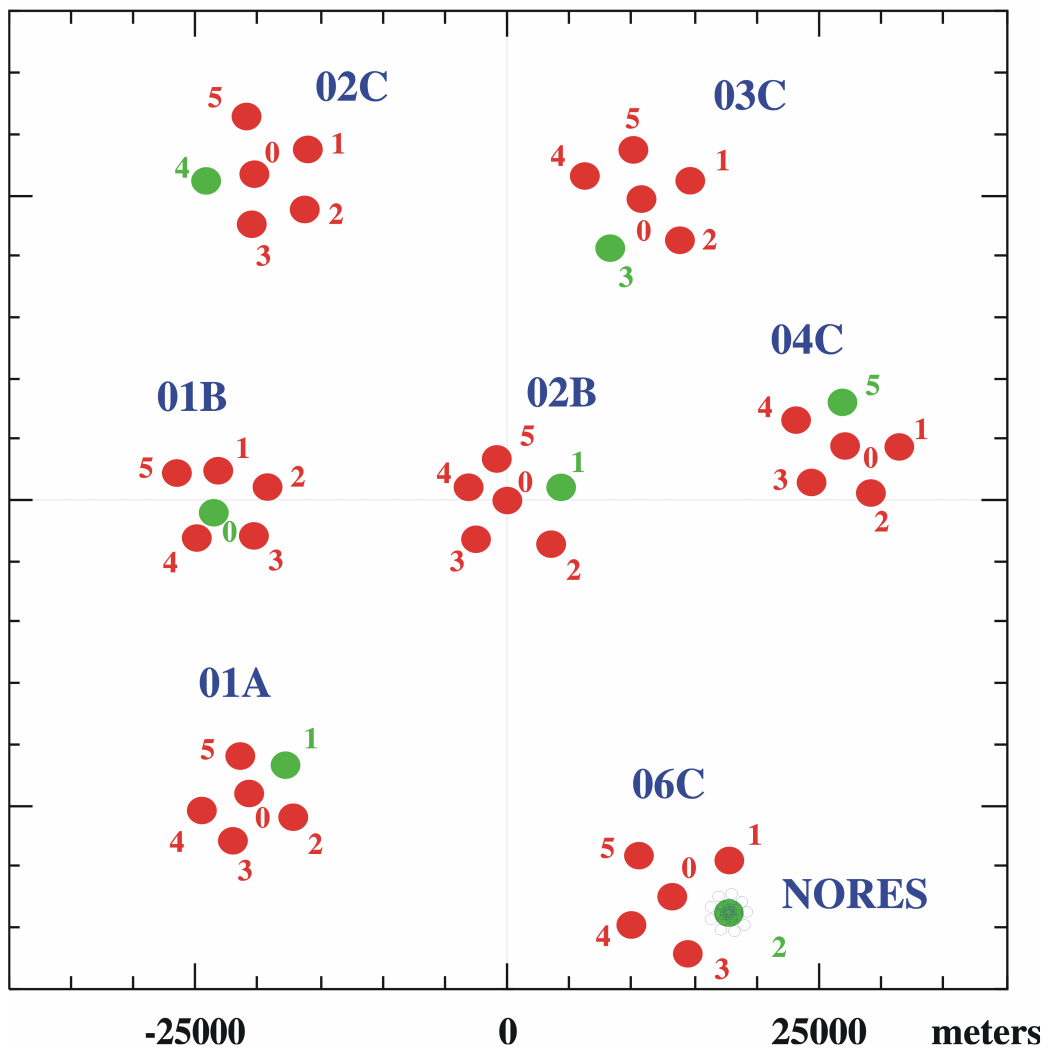


**Fig. 9.2** Configuration of the large aperture array NORSAR and the small aperture array NORES. The NORES array is co-located with the NORSAR subarray 06C. The diameter of NORSAR is about 60 km and the diameter of NORES is about 3 km. Each seismometer site is marked with a circle. The present NORSAR array has 42 sites, whereas the NORES array has 25 sites. The NORSAR array has logically seven subarrays, each with six vertical seismometers. In addition, one site in each subarray (marked in green) has one three-component broadband seismometer. The geometry of NORES is identical to the geometry of ARCES shown in Fig. 9.1. The center seismometer of the NORSAR subarray 02B has the geographic coordinates  $61.03972^{\circ}\text{N}$ ,  $11.21475^{\circ}\text{E}$ . The center seismometer of NORES has the geographic coordinates  $60.73527^{\circ}\text{N}$ ,  $11.54143^{\circ}\text{E}$ .

## 9. Seismic Arrays

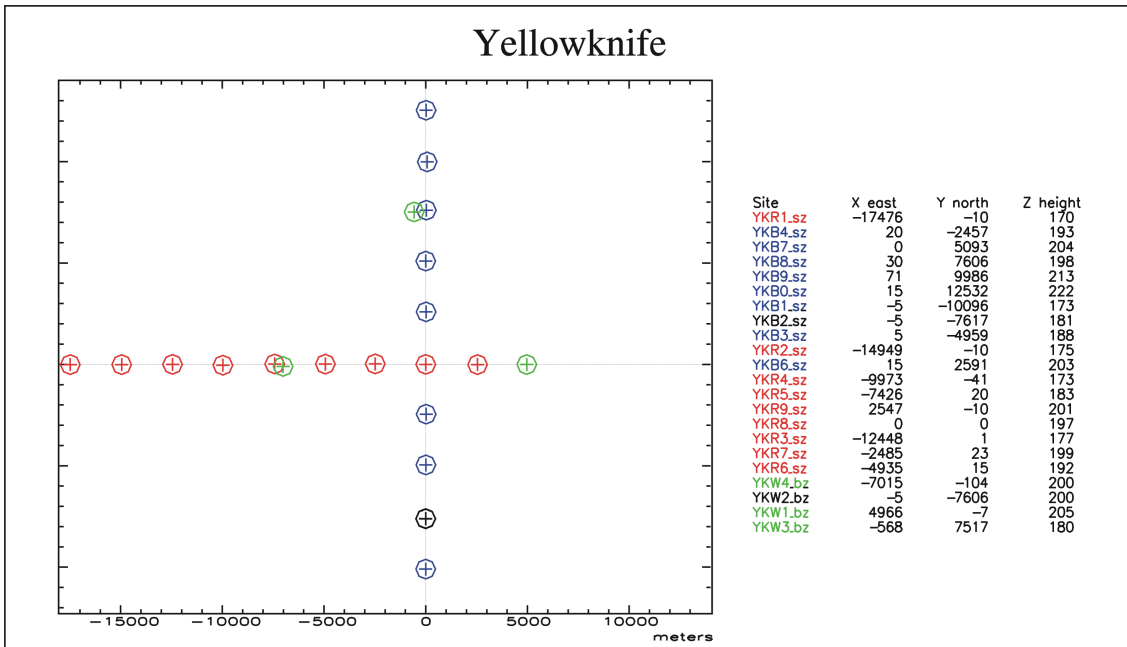


**Fig. 9.3** Configuration of the United Kingdom Atomic Energy Agency - type Yellowknife array (YKA). The blue and the red sites have vertical short-period instruments, and at the green sites, three-component, broadband seismometers are installed.

The large LASA and NORSAR arrays and the UKAEA arrays have narrow band short-period seismometers and additional long-period seismometers in their original configuration, whereas the Gräfenberg Array (GRF) was planned and installed in the early 1970s as an array of broadband sensors. It has an aperture of about 100 km (Harjes and Seidl, 1978; Buttkus, 1986) and an irregular shape (Fig. 9.4), which follows the limestone plateau of the Franconian Jura.

However, the geometry and the number of seismometer sites of an array are determined by economy and purpose. Details about array configurations can be found in Haubrich (1968), Harjes and Henger (1973), or in Mykkeltveit et al. (1983, 1988).

Tab. 9.3 in 9.10 contains a list of operational and planned arrays as of September 2002, and Fig. 9.42 shows a map of these array locations.

Spudich and Bostwick (1987) used the principle of reciprocity and used a cluster of earthquakes as a source array to analyze coherent signals in the seismic coda. This idea was consequently expanded by Krüger et al. (1993) who analyzed data from well-known source locations (i.e., mostly explosion sources) with the so-called “double beam method”. Here the principle of reciprocity for source and receiver arrays is used to further increase the resolution by combining both arrays in one analysis.

Another approach to arrays with high resolution was developed in recent years. In Japan and in California the network of seismometer stations is so dense that data from all stations can be combined in the so-called J-array and the Californian array. All known array techniques can be applied to analyze data from these networks (J-array Group, 1993, Benz et al., 1994).

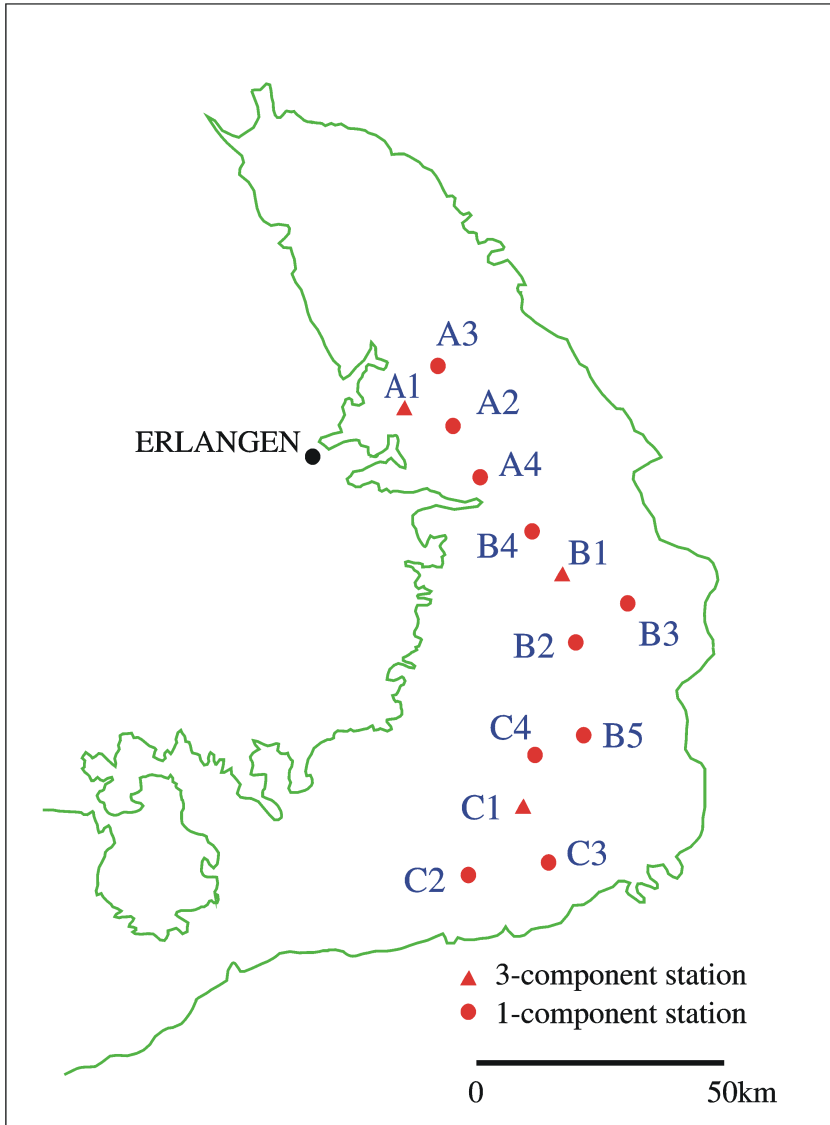


**Fig. 9.4** Configuration of the irregularly shaped Gräfenberg array (GRF). At all sites vertical broadband seismometers are installed. In addition, three sites (A1, B1, and C1) contain horizontal broadband seismometers. The contour line follows the boundary of the geological unit of the Franconian Jura, on which the array is located. The reference station GRA1 (at position A1 on the map) is sited at latitude 49.69197°N and longitude 11.22200°E.

## 9.4 Array beamforming

With an array we can improve the signal-to-noise ratio (SNR) of a seismic signal by summing the coherent signals from the single array sites. Figs. 9.5 and 9.6 show P onsets of a regional event observed at the ARCES sites and, in addition, the summation trace (on top) of all single observations. In Fig. 9.5 the data were summed without taking any delay times into account, consequently the P onset is suppressed by destructive interference. In Fig. 9.6 all traces were time-adjusted to provide alignment of the first P pulse before summation. Note the sharp and short P pulse of the beam and the suppression of incoherent energy in the P coda.

## 9. Seismic Arrays

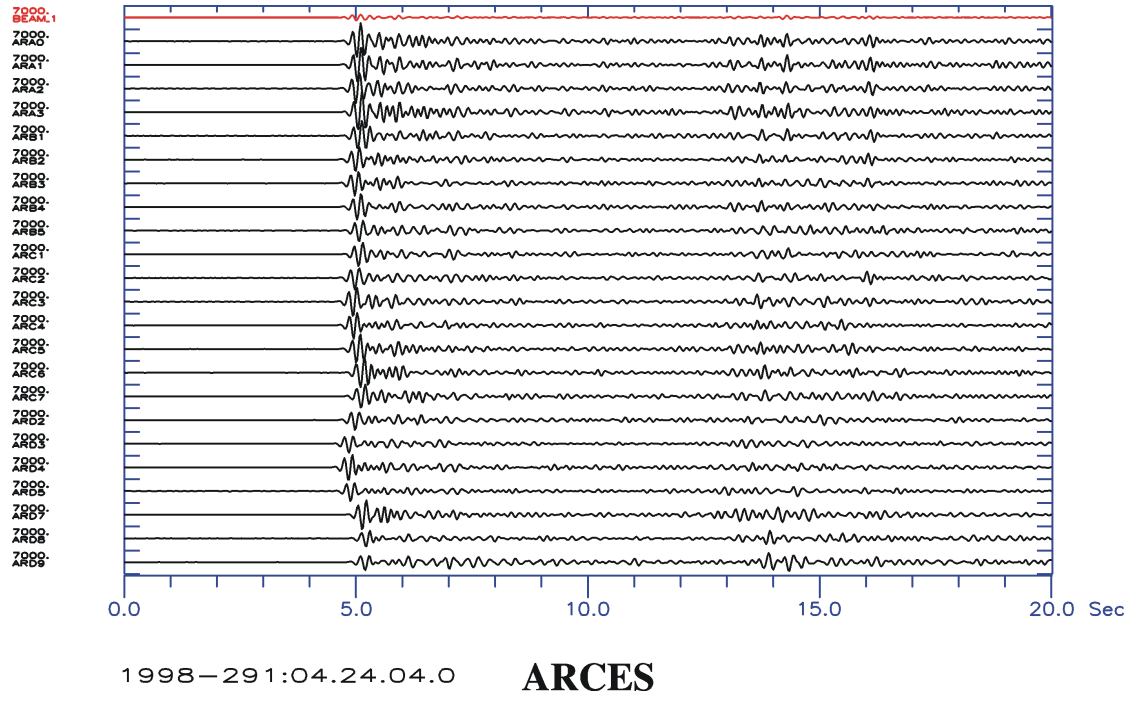


**Fig. 9.5** The figure shows P-phase onsets of a regional event observed with the vertical short-period seismometers of ARCES. The top trace is an array beam, and the remaining traces are single vertical short-period seismograms. All data were filtered with a Butterworth band pass filter between 4 and 8 Hz and are shown with a common amplification. All traces were summed to create a beam (red trace) without any delay-time application.

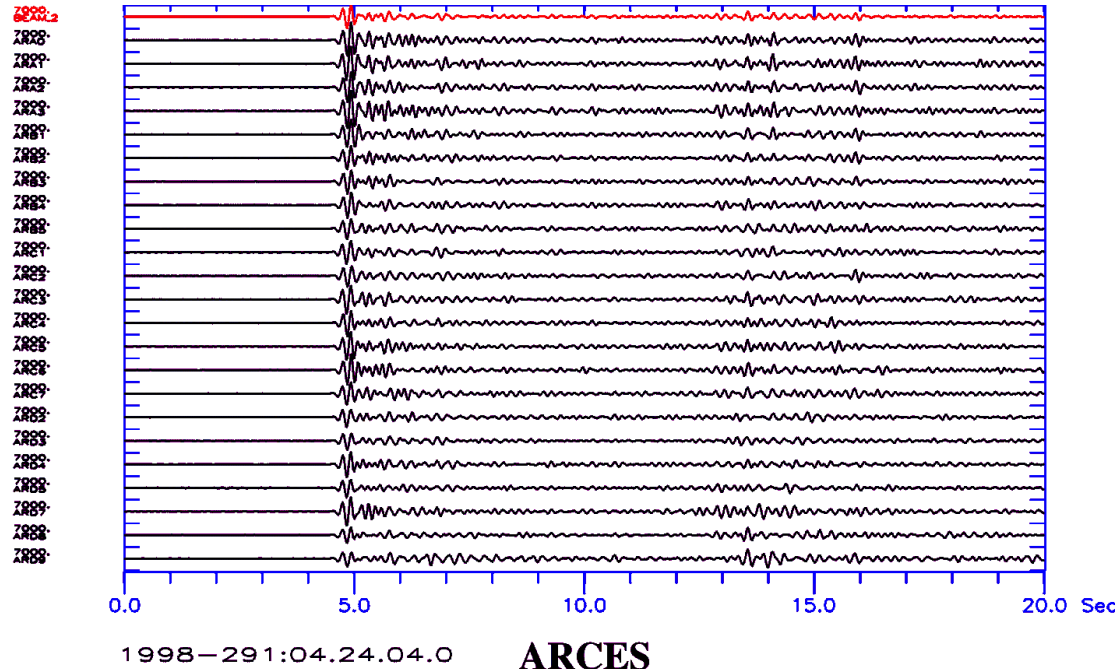


**Fig. 9.6** This figure shows P-phase onsets of a regional event observed with the vertical short-period seismometers of ARCES as in Fig. 9.5 but the single traces were first aligned and then summed (beam trace in red). Note for this case the sharp and short pulse form of the first P onset of the beam and the suppression of incoherent energy in the P coda.

This shows that the most important point during the summation (or beamforming) process is to find the best delay times, with which the single traces must be shifted before summation (“delay and sum”) in order to get the largest amplitudes due to coherent interference of the signals. The simplest way is just to pick the onset times of the signal on each trace and shift the traces with respect to the onset time at the reference site of the array. But most onsets from weaker events have a much smaller SNR than in the example shown, and therefore onset times are often difficult to pick. With hundreds of onsets each day, this is not practical during routine operation of an array. Therefore, many different predefined beams are automatically calculated, and a detector then searches for interesting onsets in these beams.

Below, we explain how delay times can be theoretically calculated for known seismic signals, using some basic equations and parameter definitions, and give the formulas for a seismic beam.

### 9.4.1 Geometrical parameters

An array is defined by a set of seismometers with one seismometer being assigned the role of a reference site. The relative distances from this reference point to all other array sites are used later in all array specific analysis algorithms (Fig. 9.7).

$\mathbf{r}_j$  Position vector of instrument  $j$  with a distance (absolute value)  $r_j$  from a defined origin. We use bold characters for vectors and normal characters for scalars. The position is normally given relative to a central instrument at site  $O$ ,  $\mathbf{r}_j = f(x, y, z)$ , where  $(x, y, z)$  are the Cartesian coordinates in [km] with positive axes towards east ( $x$ ), towards north ( $y$ ), and vertically above sea level ( $z$ ).

For distances from the source much larger than the array aperture (i.e., more than about 10 wavelengths) a seismic wave approaches an array with a **wavefront** close to a **plane**. The case of a non-plane wavefront is discussed in Almendros et al. (1999). The directions of approach and propagation of the wavefront projected on to the horizontal plane are defined by the angles  $\Phi$  and  $\Theta$  (Fig. 9.8).

- Φ Backazimuth (often abbreviated as BAZ or for short, called azimuth) = angle of wavefront approach, measured clockwise between the north and the direction towards the epicenter in [ $^{\circ}$ ].
- Θ Direction in which the wavefront propagates, also measured in [ $^{\circ}$ ] from the north with  $\Theta = \Phi \pm 180^{\circ}$ .

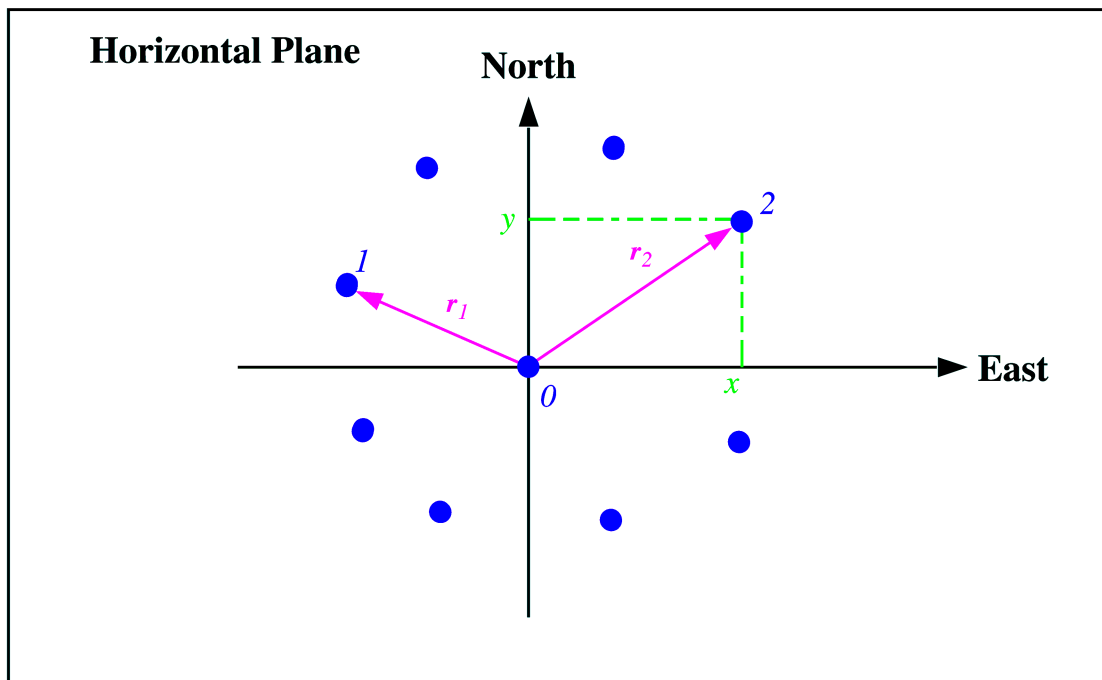


**Fig. 9.7** Illustration (horizontal plane) of an array of instruments (filled circles). The center instrument  $O$  is used as reference and origin for the relative coordinates  $x$ ,  $y$  (see also Fig. 9.1 for an example of an actual array).

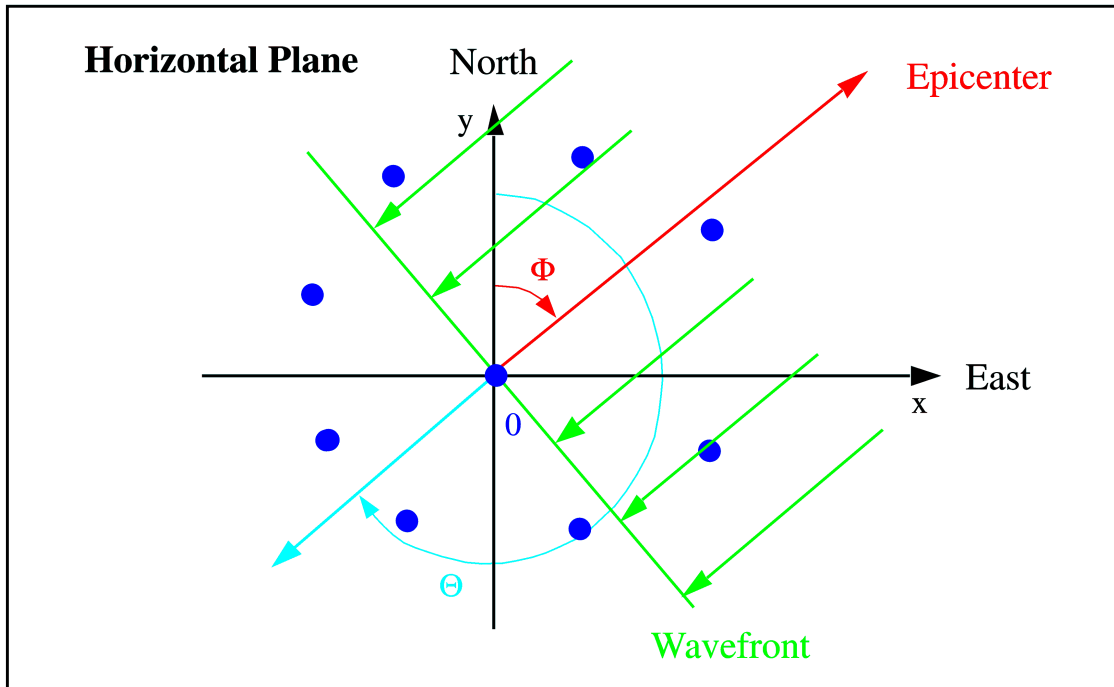


**Fig. 9.8** Definition of the angles  $\Theta$  (direction of wavefront propagation) and  $\Phi$  (direction to the epicenter = backazimuth); here e.g., for a wavefront coming from north-east and crossing the array in a south-westerly direction.

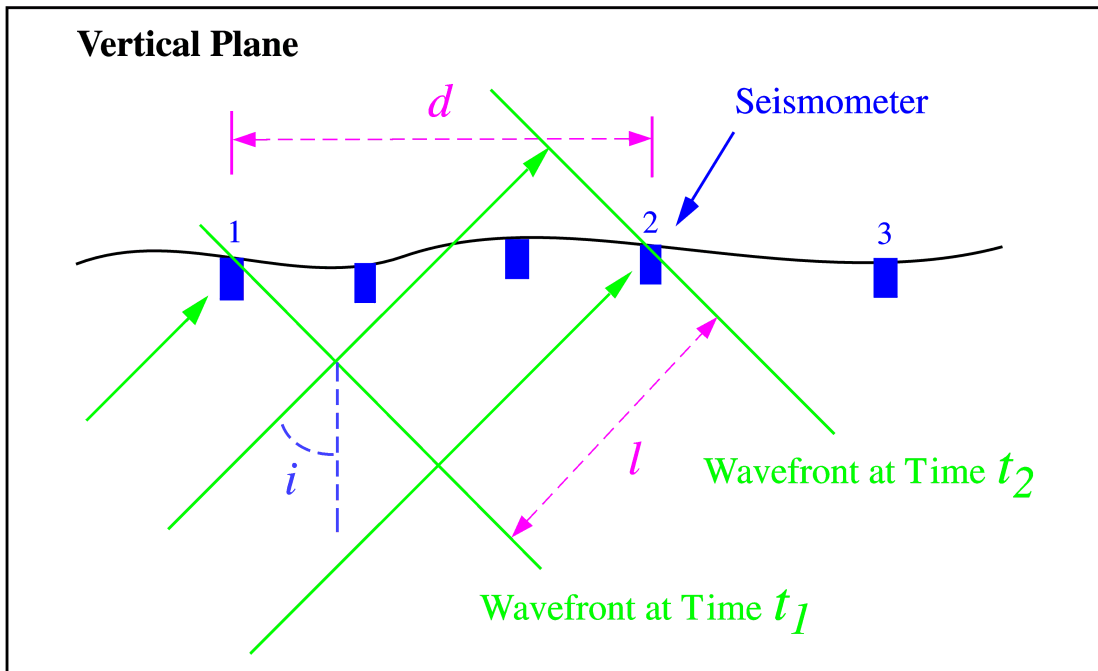


**Fig. 9.9** Illustration (vertical plane) of a seismic plane wave crossing an array at an angle of incidence  $i$ .

In the vertical plane, the angle measured between the direction of approach and the vertical is called the angle of incidence  $i$  with  $i \leq 90^\circ$  (see Fig. 9.9). The seismic velocity below the array in the uppermost crust and the angle of incidence define the apparent propagation speed of the wavefront crossing the array.

#### 9.4.2 Apparent velocity and slowness

The upper crustal velocity together with the angle of incidence defines the apparent propagation speed of the wavefront at the observing instruments. This is **not** the physical propagation speed of the wavefront and is therefore called an apparent velocity. We start our consideration by defining the quantities used in following:

- $d$  horizontal distances;
- $v_c$  crustal velocity (P or S wave, depending on the seismic phase) immediately below the array in [km/s];
- $i$  angle of incidence (see also Fig. 9.9);
- $v_{app}$  absolute value of the apparent velocity vector in [km/s] of a plane wave crossing an array. Using Snell's law it can easily be proven that the apparent velocity is a constant for a specific seismic ray traveling through a horizontally layered Earth model (see Fig. 9.10);
- $\mathbf{v}_{app}$  apparent velocity vector with its absolute value  $v_{app} = 1/s$ .  $\mathbf{v}_{app} = (v_{app,x}, v_{app,y}, v_{app,z})$ , where  $(v_{app,x}, v_{app,y}, v_{app,z})$  are the single, apparent velocity components in [km/s] of the wavefront crossing an array.

## 9. Seismic Arrays

The inverse of the apparent velocity  $v$  is called slowness  $s$ , which is a constant for a specific ray. For local or regional applications the unit of slowness is [s/km]. For global applications it is more appropriate to use the unit [ $s/\circ$ ] and the slowness is then called the ray parameter. The ray parameter of major seismic phases is usually tabulated for standard Earth models together with the travel times as a function of distance from the source. The following symbols are used:

- $s$  slowness vector with its absolute value  $s = 1/v_{app}$ .  $s = (s_x, s_y, s_z)$ , where  $(s_x, s_y, s_z)$  are the single, inverse apparent velocity (= slowness) components in [s/km]. Note, because the vector  $s$  is oriented in the propagation direction (in direction of  $\Theta$ , see Fig. 9.8), a plane wave with backazimuth  $45^\circ$  would have negative values for both horizontal components;
- $s$  absolute value of the slowness vector in [s/km] of a plane wave crossing an array;
- $p$  ray parameter  $p = s \cdot g$ , measured in [ $s/\circ$ ], with  $g = \frac{\pi \cdot 6371 \text{ km}}{180^\circ} \cong 111.19 \text{ [km/\circ]}$ .

The relation between the parameters of a plane wave and the actual seismic signal is given by the wavenumber vector  $k$ :

- $k$  wavenumber vector defined as  $k = \omega \cdot s$  with the angular frequency  $\omega = 2 \cdot \pi \cdot f = 2 \cdot \pi / T$  measured in [1/s].  $T$  is the period and  $f$  the frequency of the seismic signal;
- $k$  absolute value of the wavenumber vector  $k$  defined as  $k = \omega \cdot u = 2 \cdot \pi \cdot f \cdot s = 2 \cdot \pi / \lambda$ , measured in [1/km].  $\lambda$  is the wavelength of the signal and because of the analogy between  $\omega$  and  $k$ ,  $k$  is also called a spatial frequency.

A time delay  $\tau_j$  is the arrival time difference of the wavefront between the seismometer at site  $j$  and the seismometer at the reference site. The unit of measurement is seconds with a positive delay meaning a later arrival with respect to the reference site in the direction of the wave propagation  $\Theta$ .

Assume a wavefront is propagating the distance  $l$  between time  $t_1$  and time  $t_2$  (Fig. 9.9). Then, if  $d$  is used for the horizontal distance between instrument 1 and 2 in [km], and if both instruments are assumed to be at the same elevation, we have:

$\tau_2 = (t_2 - t_1) = \frac{l}{v_c}$ , and the apparent velocity  $v_{app}$  is then defined as a function of the incidence angle  $i$  (Fig. 9.10):

$$v_{app} = \frac{d}{(t_2 - t_1)} = \frac{v_c}{\sin i} \quad (9.1)$$

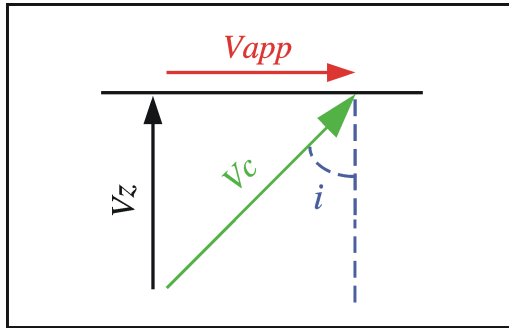


**Fig. 9.10** A plane wave propagating with the velocity  $v_c$  reaches the Earth's surface. The splitting of this velocity in a vertical component  $v_z$  and a horizontal component  $v_{app}$  is directly dependent on the incidence angle  $i$ . The horizontal velocity component is only equal to the propagation velocity  $v_c$  for waves propagating parallel to the surface; in all other cases  $v_{app}$  is higher than  $v_c$ . It is called the apparent velocity  $v_{app}$  of the seismic wave.

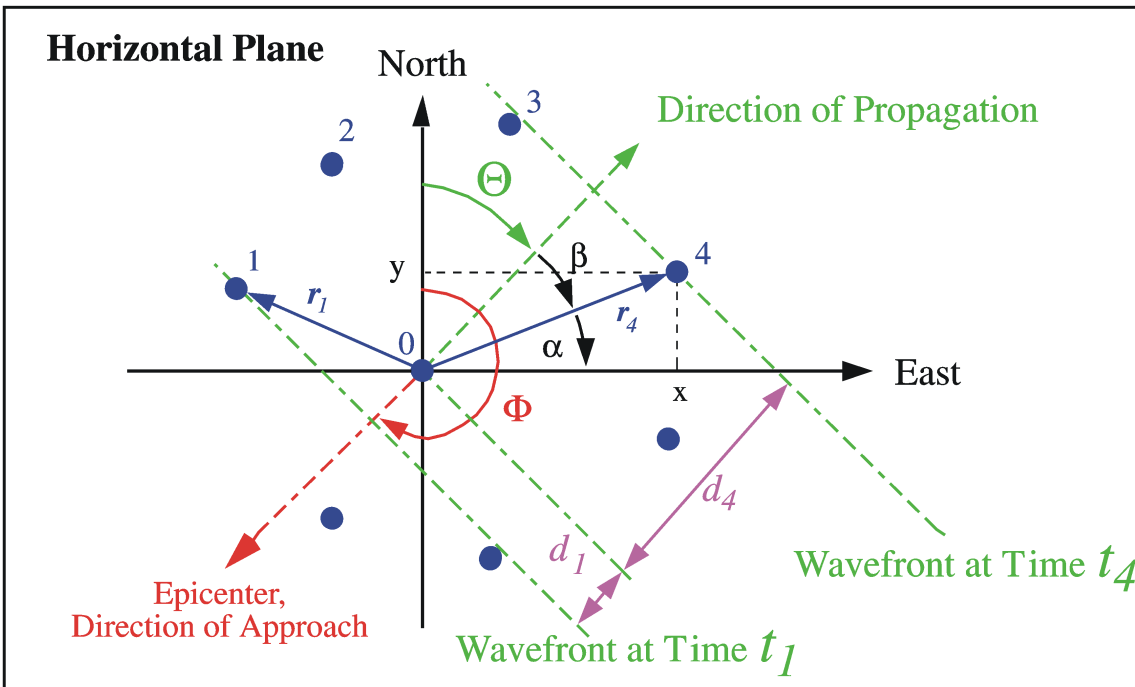


**Fig. 9.11** Illustration (horizontal plane) of a plane wave, coming from south-west (backazimuth  $\Phi$ ), crossing an array and propagating in a north-easterly direction  $\Theta$ .

### 9.4.3 Plane-wave time delays for sites in the same horizontal plane

In most cases, the elevation differences between the single array sites are so small that travel-time differences due to elevation differences are negligible (Fig. 9.9). We can assume, therefore, that all sites are in the same horizontal plane. In this case, we can not measure the vertical component of the wavefront propagation. The vertical apparent velocity component can then be defined as  $v_{app,z} = \text{infinite}$ , and the corresponding slowness component becomes  $s_z = 0$ . From Fig. 9.11 we see that the time delay  $\tau_4$  [s] between the center site 0 and site 4 with the relative coordinates  $(x_4, y_4)$  is

## 9. Seismic Arrays

$$\tau_4 = \frac{d_4}{v_{app}} = \frac{r_4 \cdot \cos \beta}{v_{app}}, \text{ with } r_4 = |\mathbf{r}_4|.$$

Now let us omit the subscript 4, and evaluate further:

$$\begin{aligned} \alpha + \beta + \Theta &= 90^\circ, \quad r \cdot \cos \beta = d, \quad r \cdot \cos \alpha = x, \quad d = \frac{x \cdot \cos \beta}{\cos \alpha} \\ d &= \frac{x \cdot \cos(90^\circ - \alpha - \Theta)}{\cos \alpha} = \frac{x \cdot (\sin \alpha \cdot \cos \Theta + \cos \alpha \cdot \sin \Theta)}{\cos \alpha} = x \cdot \frac{\sin \alpha}{\cos \alpha} \cdot \cos \Theta + x \cdot \sin \Theta \\ d &= x \cdot \frac{y}{x} \cdot \cos \Theta + x \cdot \sin \Theta = y \cdot \cos \Theta + x \cdot \sin \Theta \end{aligned}$$

With  $\Theta = \Phi \pm 180^\circ$  (Fig. 9.8), we get for the horizontal distance traveled by the plane wave  $d = -x \cdot \sin \Phi - y \cdot \cos \Phi$ .

Then, for any site  $j$  with the horizontal coordinates  $(x, y)$ , but without an elevation difference relative to the reference (center) site, we get the time delay  $\tau_j$ :

$$\tau_j = \frac{d_j}{v_{app}} = \frac{-x_j \cdot \sin \Phi - y_j \cdot \cos \Phi}{v_{app}} \quad (9.2)$$

These delay times can also be written in the often-used formal vector syntax with the position vector  $\mathbf{r}_j$  and the slowness vector  $\mathbf{s}$  as parameters. In this notation the delay times are defined as projection of the position vector onto the slowness vector:

$$\tau_j = \mathbf{r}_j \cdot \mathbf{s} \quad (9.3)$$

### 9.4.4 Plane-wave time delays when including the elevation of sites

In some cases, not all array sites are located in one plane. Then the calculation of the time delays becomes slightly more complicated. Site 2 has the relative coordinates  $(x_2, y_2, z_2)$ . From Fig. 9.12 we see that  $i + \gamma + \phi = 90^\circ$ ,  $z_2 = r_2 \cdot \sin \phi$ ,  $d_2 = r_2 \cdot \cos \phi$ ,  $l = r_2 \cdot \cos \gamma$ , and  $\tau_2 = \frac{l}{v_c}$ .

$$l = \frac{z_2}{\sin \phi} \cdot \cos \gamma = \frac{z_2}{\sin \phi} \cdot \cos(90^\circ - i - \phi) = \frac{z_2 \cdot (\sin i \cdot \cos \phi + \cos i \cdot \sin \phi)}{\sin \phi}$$

Omitting again the site number, we get:

$$l = z \cdot \frac{\cos \Phi}{\sin \varphi} \cdot \sin i + z \cdot \cos i = d \cdot \sin i + z \cdot \cos i$$

Using Eq. (9.1) and Eq. (9.2), we get for the total time delay at site  $j$

$$\tau_j = \frac{-x_j \cdot \sin i \cdot \sin \Phi - y_j \cdot \sin i \cdot \cos \Phi + z_j \cdot \cos i}{v_c} = \frac{-x_j \cdot \sin \Phi - y_j \cdot \cos \Phi}{v_{app}} + \frac{z_j \cdot \cos i}{v_c} \quad (9.4)$$

The time delays  $\tau_j$  now also depend on the local crustal velocities below the given site  $j$  and not just on the parameters of the wavefront ( $\Phi, v_{app}$ ). This is a clear disadvantage of an array for which single sites are not located in one horizontal plane and should be taken into account during planning of an array installation. Writing these time delays in vector notation will again result in Eq. (9.3), but note, the vectors are now three-dimensional.

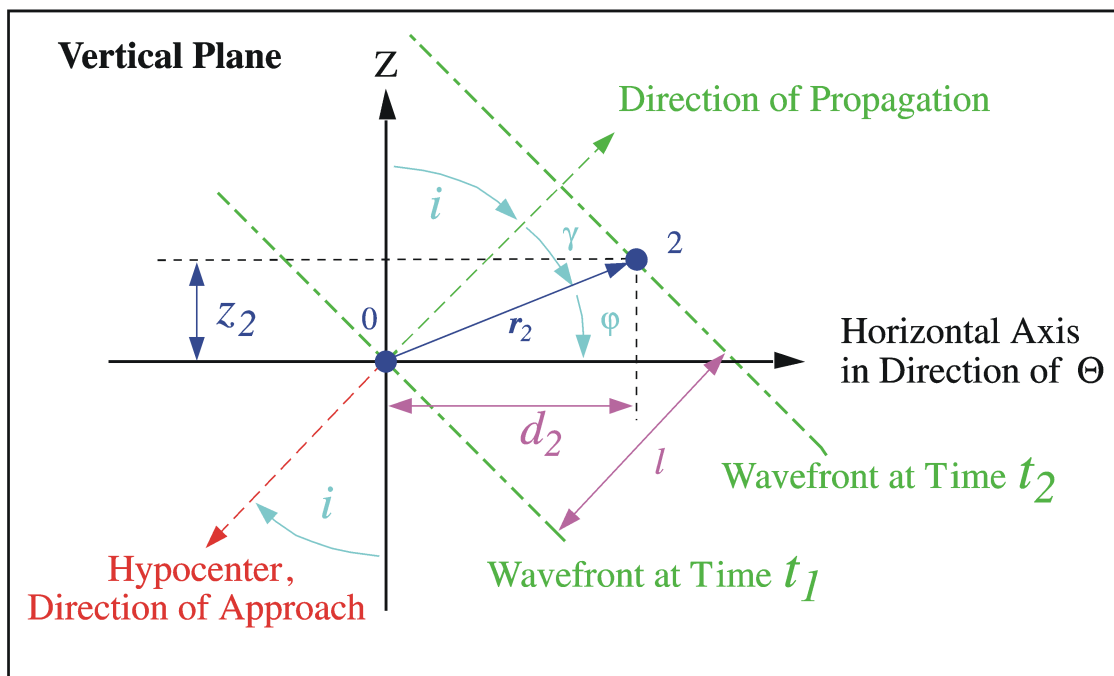


**Fig. 9.12** Illustration (vertical plane) of a plane wave crossing an array at the angle of incidence  $i$ .

#### 9.4.5 Beamforming

After deriving the delay times  $\tau_j$  for each station by solving Eq. (9.2) or Eq. (9.4) for a specific backazimuth and apparent velocity combination, we can define a “delay and sum” process to calculate an array beam. In the following we will use the shorter vector syntax of Eq. (9.3) to calculate time delays. The calculated delay times can be negative or positive. This is depending on the relative position of the single sites with respect to the array’s reference point and to the backazimuth of the seismic signal. Negative delay times correspond to a delay and positive delay times correspond to an advance of the signal.

## 9. Seismic Arrays

Let  $w_j(\mathbf{r}_j, t)$  be the digital sample of the seismogram from site  $j$  at time  $t$ , then the beam of the whole array is defined as

$$b(t) = \frac{1}{M} \sum_{j=1}^M w_j(t + \mathbf{r}_j \cdot \mathbf{s}) = \frac{1}{M} \sum_{j=1}^M w_j(t + \tau_j). \quad (9.5)$$

This operation of summing the recordings of the  $M$  instruments by applying the time delays  $\mathbf{r} \cdot \mathbf{s}$  is called beamforming.

Because we are using digitized data, sampled with a defined sampling rate, we will always need an integer number of samples in programming Eq. (9.5), that is, the term  $t + \mathbf{r}_j \cdot \mathbf{s} = t + \tau_j$  needs to be converted to an integer sample number. However, to avoid alias effects by following the rules of digital signal processing, it is sufficient for beamforming to use the nearest integer sample, as long as the dominating frequency is less than 25% of the sampling rate.

If seismic waves were harmonic waves  $S(t)$  without noise, with identical site responses, and without attenuation, then a “delay and sum” with Eq. (9.5) would reproduce the signal  $S(t)$  accurately. The attenuation of seismic waves within an array is usually negligible, but large amplitude differences can sometimes be observed between data from different array sites due to differences in the crust directly below the sites (see Fig. 4.34). In such cases, it can be helpful to normalize the amplitudes before beamforming.

Our observations  $w(t)$  are, of course, the sum of background noise  $n(t)$  plus signal  $S(t)$ , i.e.,  $w(t) = S(t) + n(t)$ .

The actual noise conditions and signal amplitude differences will influence the quality of a beam. However, because the noise is usually more incoherent than the signal, we can try to estimate the improvement of the signal-to-noise ratio (SNR) due to the beamforming process.

Calculating the beam trace for  $M$  observations including noise we get for the sum  $B$  of all traces with Eq. (9.5):

$$B(t) = \sum_{j=1}^M w_j(t + \mathbf{r}_j \cdot \mathbf{s}) = \sum_{j=1}^M (S_j(t + \mathbf{r}_j \cdot \mathbf{s}) + n_j(t + \mathbf{r}_j \cdot \mathbf{s})).$$

Assuming that the signal is coherent and not attenuated, this sum can be split and we get:

$$B(t) = M \cdot S(t) + \sum_{j=1}^M n_j(t + \mathbf{r}_j \cdot \mathbf{s}). \quad (9.6)$$

Now we assume that the noise  $n_j(\mathbf{r}_j, t)$  has a normal amplitude distribution, a zero mean value, and the same variance  $\sigma^2$  at all  $M$  sites. Then, for the variance of the noise after summation, we get  $\sigma_s^2 = M \cdot \sigma^2$  and the standard deviation of the noise in the beam trace will become  $\sqrt{M} \cdot \sigma$ . That means that the standard deviation of the noise will be multiplied only with a factor of  $\sqrt{M}$ , but the coherent signal with the factor  $M$  (Eq. (9.6)). So, the

improvement of the signal-to-noise ratio by the “delay and sum” process will be  $\sqrt{M}$  for an array containing  $M$  sites. The gain improvement  $G$  of an  $M$ -sensor array can then be written as

$$G^2 = M . \quad (9.7)$$

#### 9.4.6 Examples of beamforming

In Fig. 9.13 (top trace), we display a beam calculated by using the known apparent velocity ( $v_{app} = 10.0$  km/s and backazimuth  $158^\circ$ ) for the P-onset of an event in Greece recorded at NORES at an epicentral distance of  $21.5^\circ$ . All 25 vertical sensors of the array have been used, but only a few of the sensors in the NORES D-ring have been displayed. Note that the signal on the beam is very similar to the individual signals, but the noise changes both in frequency content and amplitude level. The beam is made by calculating time delays for the given slowness using Eq. (9.2), and in the summation of the traces, the individual traces have been shifted with these delays.

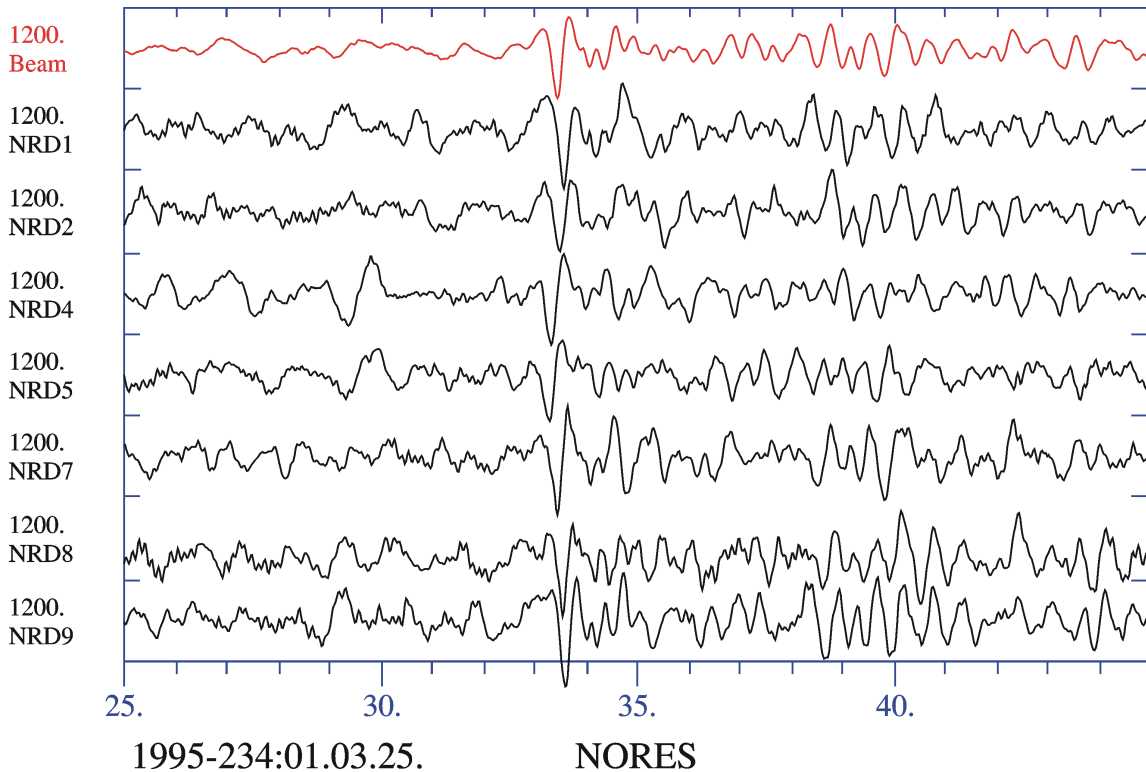


**Fig. 9.13** Selected NORES channels from an event in Greece, with the beam displayed as the top trace (in red). All traces have equal amplitude scale.

The next example in Fig. 9.14 shows the ability of arrays to detect small signals that are difficult to detect with single stations. It shows the tiny onset of a P<sub>cP</sub> phase recorded at the GERES array from a deep focus event in the Tyrrhenian Sea ( $h = 275$  km) at an epicentral distance of  $9.6^\circ$ . Note that although the signal coherence is low, the noise suppression on the beam is clearly visible and the onset can be analyzed. For the “delay and sum” process, data from 20 sites of the GERES array were used, but only a subset of the single traces is shown.

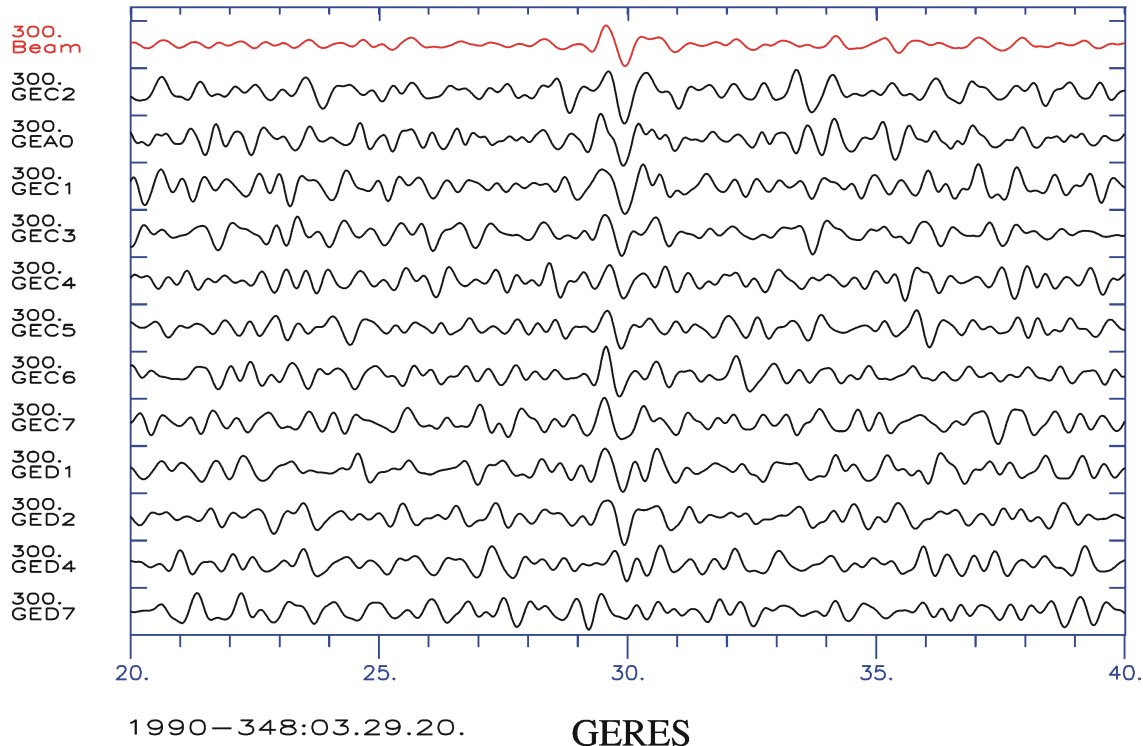


**Fig. 9.14** GERES beam (top trace in red) for a Pcp onset observed at an epicentral distance of  $9.6^\circ$  from a deep focus event in the Tyrrhenian Sea.

## 9.5 Beamforming and detection processing

A major task in processing seismic data is that of detecting possible signals in the data samples collected from the seismometers. A “signal” is defined to be distinct from the background noise due to its amplitudes, different shape, and/or frequency contents; in other words, the variance of the time series is increased when a signal is present. Statistically, we can form two hypotheses: the observation is noise or the observation is a signal plus noise. The signal of a plane wave observed at different sites of an array should be more coherent than random noise. If we assume that the time series recorded are independent measurements of a zero-mean Gaussian random variable, then it can be shown that the hypothesis of the recording being noise can be tested by measuring the power within a time window. If this power exceeds a preset threshold, then the hypothesis is false, i.e., the recording is signal plus noise. In practice, the threshold can not be calculated precisely and may vary with time as is true for the background noise. But an approximation to this detector in seismology is to estimate the power over a long time interval (LTA), and over a short time interval (STA). Then the ratio STA/LTA, which is usually called signal-to-noise ratio (SNR), is compared with a preset threshold. If the SNR is larger than this threshold, the status of detection is set to “true” and we are speaking about a detected seismic signal.

This kind of an STA/LTA detector was proposed by Freiberger (1963), installed and tested for the first time at LASA (van der Kulk et al., 1965), and later installed at Yellowknife (Weichert et al., 1967) and at NORSAR (Bungum et al., 1971). For complementary details on STA/LTA trigger algorithm and parameter setting in general see IS 8.1.

At NORSAR we use a sum of the absolute values rather than squared values due to computational efficiency; the difference in performance is minimal and the results are slightly more robust. The definition of the short-term average (STA) of a seismic trace  $w(t)$  is:

$$STA(t) = \frac{1}{L} \cdot \sum_{j=0}^{L-1} |w(t-j)| \quad L = \text{sampling rate} \cdot STA \text{ length}, \quad (9.8)$$

the recursive definition of the long-term average (LTA) is:

$$LTA(t) = 2^{-\zeta} \cdot STA(t-\varepsilon) + (1 - 2^{-\zeta}) \cdot LTA(t-1), \quad (9.9)$$

where  $\varepsilon$  is a time delay, typically a few seconds, and  $\zeta$  is a steering parameter for the LTA update rate. The parameter  $\varepsilon$  is needed to prevent a too early influence of the often-emergent signals on the LTA. In the case of a larger signal, the LTA may stay too long at a relatively high level and we will therefore have problems detecting smaller phases shortly after this large signal. Therefore the LTA update is forced to lower the LTA values again by the exponent  $\zeta$ .

The signal-to-noise ratio (SNR) is defined as:

$$SNR(t) = STA(t)/LTA(t). \quad (9.10)$$

The STA/LTA operator may be used on any type of seismic signals or computed traces. That means, the input time series  $w(t)$  may be raw data, a beam, filtered data or a filtered beam.  $L$  is the number of points of the time series  $w(t)$  to be integrated. The recursive formula for the LTA means that the linear power estimate of the noise is based mainly on the last minute's noise situation, which is a very stable estimate. The influence of older noise conditions on the actual LTA value and a weighting of the newest STA value can be defined by the factor  $\zeta$ , for which, e.g. at NORSAR, a value of 6.0 is used. It is also advisable to implement a delay of  $\varepsilon = 3$  to 5 seconds for updating the LTA as compared to STA. A simpler implementation is to estimate the LTA according to Eq. (9.8), but using an integration length that is 100 or 200 times longer for the LTA than for the STA. However, when detecting signals with frequencies above 1 Hz, it is also recommended that the LTA should not be updated during the SNR is above the detection threshold. This feature is easier to implement by using Eq. (9.9).

Fig. 9.15 and Fig. 9.16 demonstrate how the STA/LTA detector works for a single seismogram. The direct P onset of this regional event is sharp and clearly detected. However, the P coda increases the background noise for later phases and the SNR of these phases becomes very small. In this case, the advantages of using an array to detect seismic signals can be easily shown. The apparent velocities of the P onsets and the S onsets are so different that calculating the corresponding S beam will decrease the P-phase energy and amplify the S-phase energy (Fig. 9.17).

In Fig. 9.18, we display again the Greek event from Fig. 9.13 with the “best” beam ( $v_{app} = 10.0$  km/s, backazimuth  $158^\circ$ ) on top, together with beams using the same apparent velocity of 10.0 km/s but different backazimuths ( $0.0^\circ$ ,  $90.0^\circ$ ,  $180.0^\circ$  and  $270.0^\circ$ ). Note the difference in amplitudes of the beams for signal and noise. Because the “best” backazimuth of  $158^\circ$  is close to  $180.0^\circ$ , the top trace and the second trace from the bottom differ only slightly.

## 9. Seismic Arrays

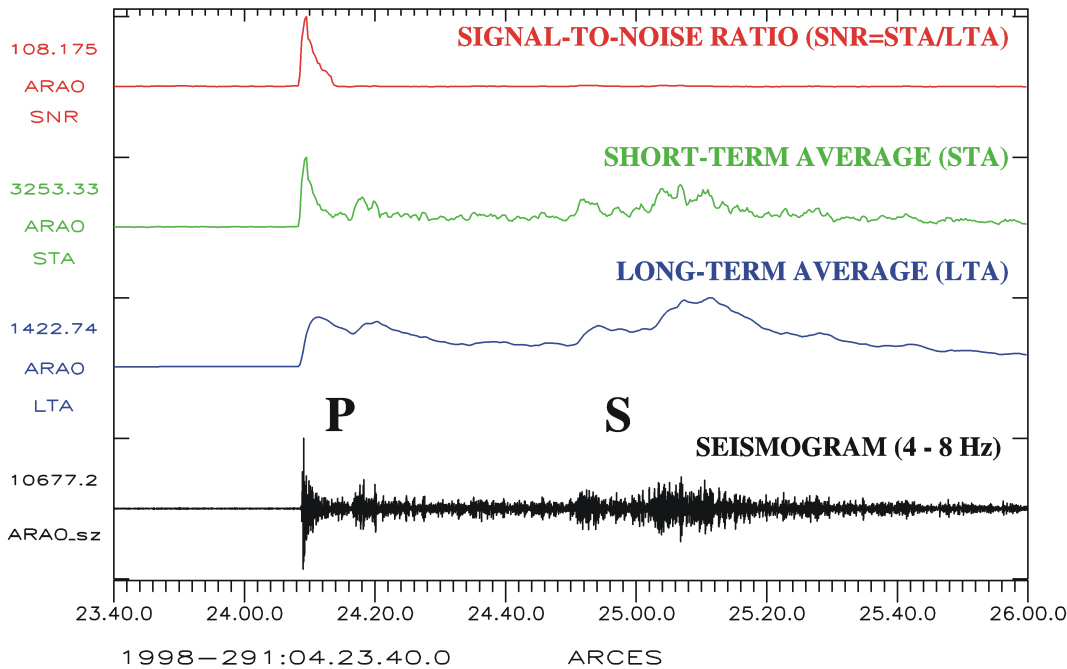


**Fig. 9.15** The figure shows the LTA, STA and STA/LTA (= SNR) traces for a seismogram of a regional event observed at the ARCES reference site ARA0 (bottom). The seismogram was bandpass filtered between 4 and 8 Hz. Note the sharp onset for the P phase with an SNR of 108.175.

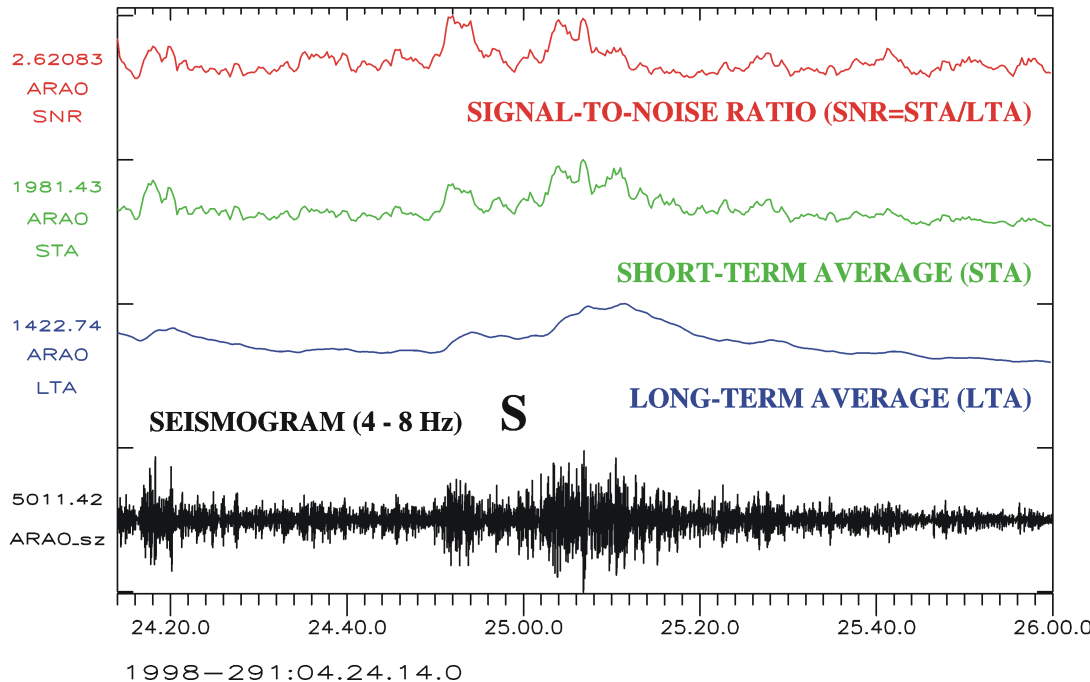


**Fig. 9.16** As Fig. 9.15, but only for the time window after the direct P onset. Note that due to the P coda the noise and consequently the LTA is increased. Therefore the SNR of the S-phase onsets becomes relatively small on this single vertical trace.

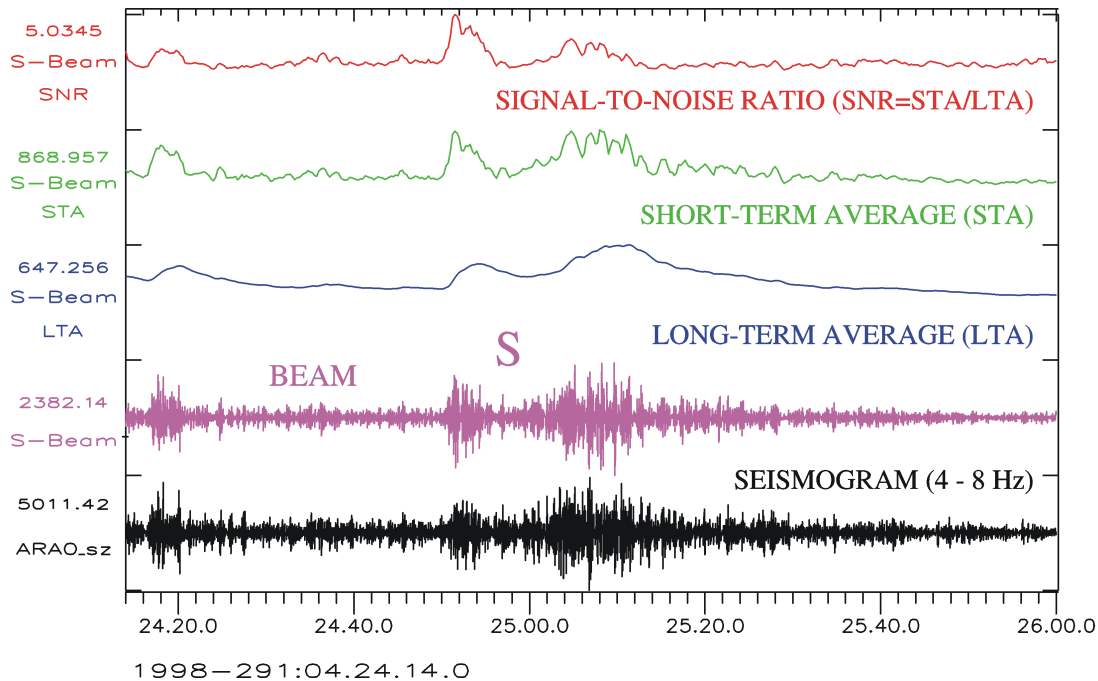


**Fig. 9.17** As Fig. 9.16, but with LTA, STA and SNR calculated for a beam optimized for the first S onset. The beam is shown as the second trace from the bottom. Compare the relative amplitudes of the P-coda on the array beam and on the single station seismogram at ARA0, which is shown at the bottom.

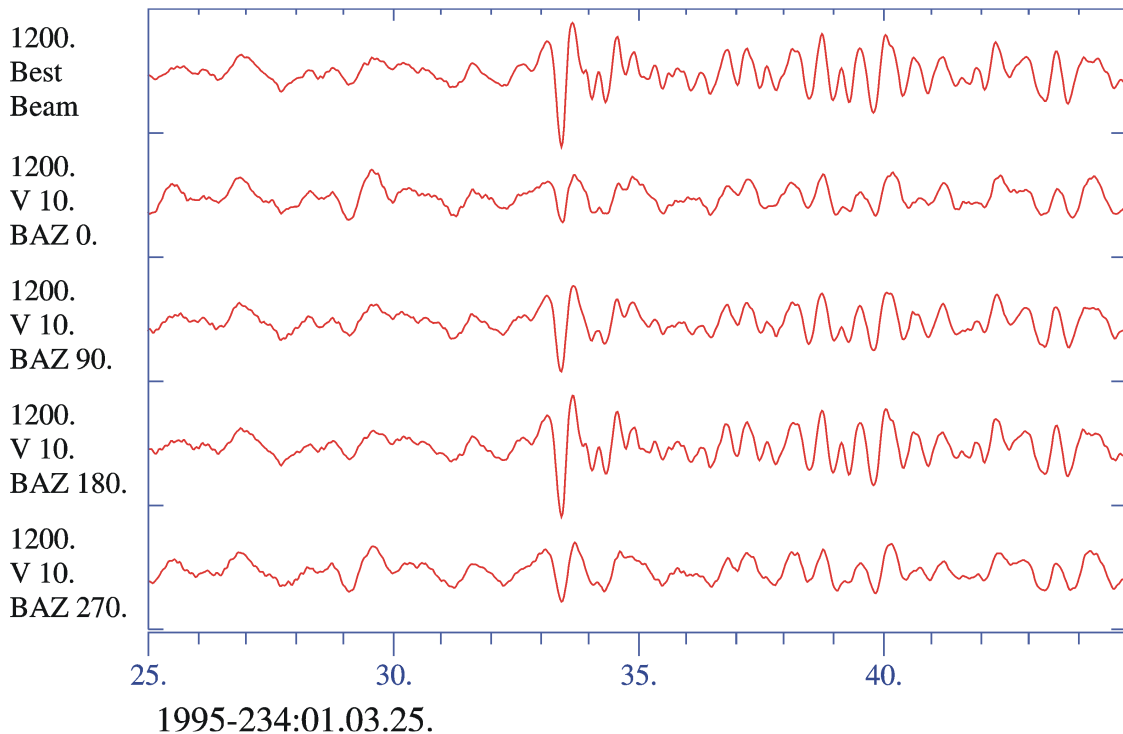


**Fig. 9.18** NORES beams for the same event as in Fig. 9.13 with different slownesses. All traces have an equal amplitude scale and show unfiltered short-period data.

Thus, Fig. 9.18 demonstrates the **limits of the slowness resolution** for small aperture arrays like NORES. To find the “best” beam is, in principle, a matter of forming beams with different slowness vectors and comparing the amplitudes or the power of the beams, and then finding which  $v_{app}$ -backazimuth combination gives the highest energy on the beam.

In Fig. 9.19, the same beams as in Fig. 9.18 are shown, but now filtered using a Butterworth 3rd order bandpass filter 2.0 – 4.0 Hz. When beamforming using Eq. (9.5), we can either filter all the individual traces first and then beamform, or we can beamform first, and then filter the beam, which is faster by a factor given by the number of sites minus one. Both procedures should theoretically give the same result because for both beamforming and filtering the superposition theorem of algebra is true. However, local noise conditions at single sites can make it useful to filter the single traces first. In the array detection process, several beams are formed, and several different filters are used (see Tab. 9.2). An STA/LTA detector is used on each such beam, and as seen from Fig. 9.19, we will get a trigger on several beams. The detector will compare the maximum STA/LTA (SNR) for every beam within a (narrow) time window, and usually report only the trigger with the highest SNR. The influence of different filters on the detectability of seismic signals is also demonstrated in Fig. 9.35.

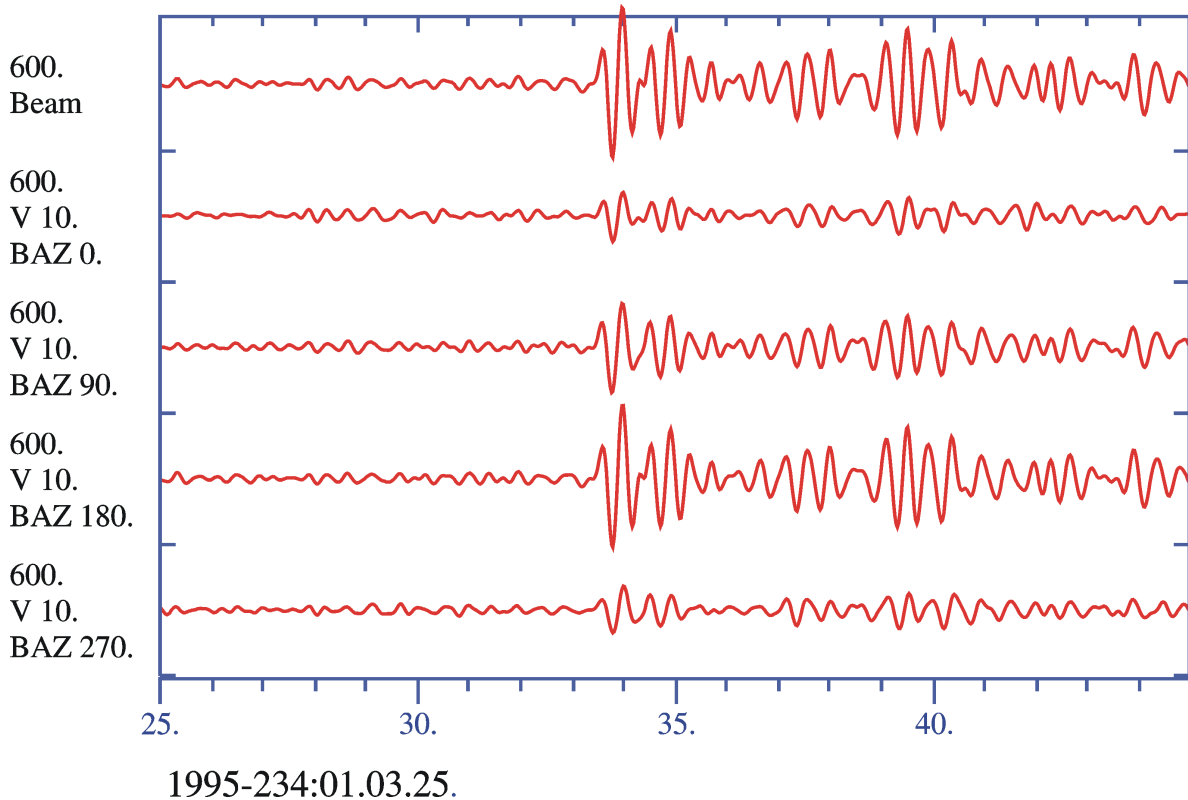


**Fig. 9.19** This figure shows the same beams as in Fig. 9.18 but filtered with a Butterworth bandpass filter 2.0 – 4.0 Hz. All traces have an equal amplitude scale.

Fig. 9.20 (top trace) shows an incoherent beam, made by first filtering the raw data, then making STA time series of each trace and afterwards, summing up the STA traces. The STA traces can be time shifted using time delays for a given slowness vector, but for detection purposes when using a small aperture array, this is not necessary since the time shifts will be very small compared to the time length of the signal. An incoherent beam will reduce the

noise variance and can be used to detect signals that are incoherent across an array. Such signals are typically of high frequency.

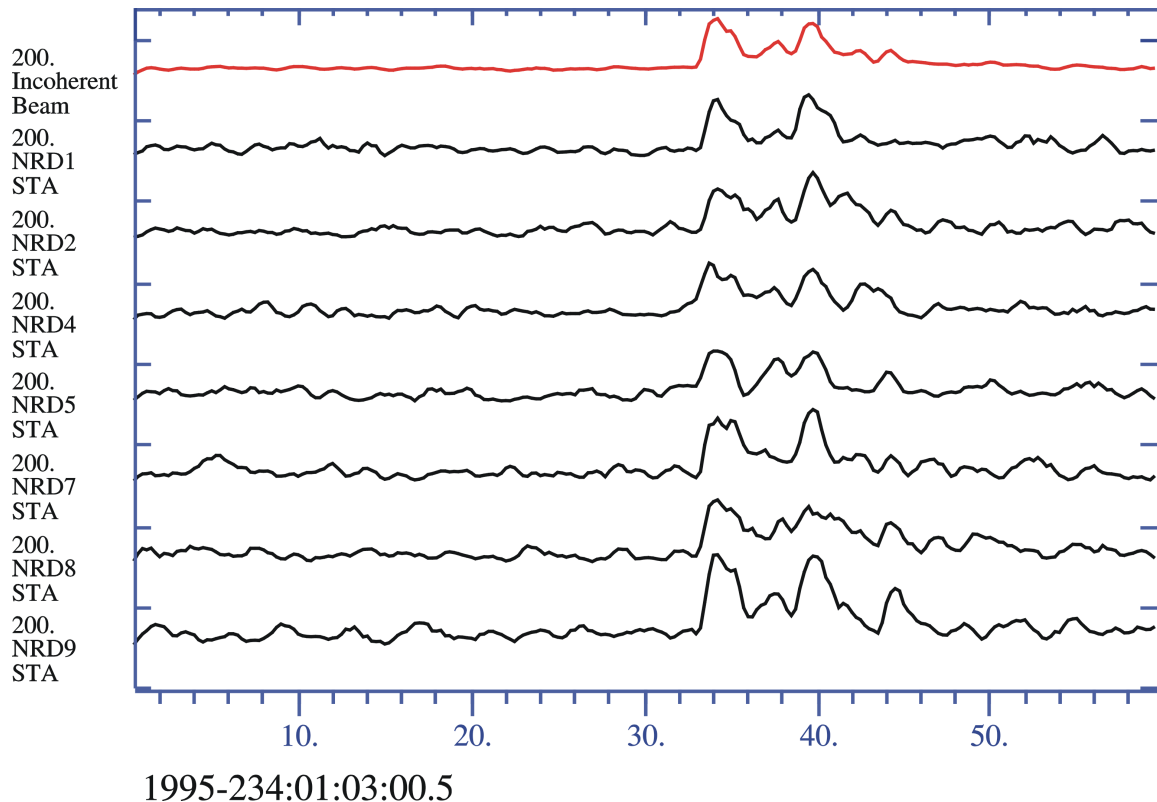


**Fig. 9.20** Illustration of an incoherent beam (see text) which is shown on top (in red). The other traces are STA time series. The selected NORES channels have been prefiltered with a Butterworth bandpass filter 2.0 – 4.0 Hz. All traces have an equal amplitude scale.

## 9.6 Array transfer function

The array transfer function describes sensitivity and resolution of an array for seismic signals with different frequency contents and slownesses. When digitizing the output from a seismometer, we are sampling the wavefront of a seismic signal in the time domain, and to avoid aliasing effects, we need to apply an anti-aliasing filter. Similarly, when observing a seismic signal using an array, we obtain a spatial sampling of the ground movement. With an array, or a dense network, we are able to observe the wavenumber  $k = 2\pi/\lambda = 2\pi \cdot f \cdot s$  of this wave defined by its wavelength  $\lambda$  (or frequency  $f$ ) and its slowness  $s$ . While analog to digital conversion may give aliasing effects in the time domain, the spatial sampling may give aliasing effects in the wavenumber domain. Therefore the wavelength range of seismic signals, which can be investigated, and the sensitivity at different wavelengths must be estimated for a given array.

A large volume of literature exists on the theory of array characteristics, e.g., Somers and Manchee (1966), Haubrich (1968), Doornbos and Husebye (1972), Harjes and Henger (1973), Harjes and Seidl (1978), Mykkeltveit et al. (1983, 1988), and Harjes (1990). How the array transfer function can be estimated will be shown in the following.

## 9. Seismic Arrays

Assuming a noise and attenuation free signal, the difference between a signal  $w$  at the reference site A and the signal  $w_n$  at any other sensor  $A_n$ , is only the onset time at which this plane wave arrives at the sensors. As we know from sub-chapter 9.4, a plane wave is defined by its propagation direction and its apparent velocity, or in short by its slowness vector  $s_o$ . Thus we can write:

$$w_n(t) = w(t - \mathbf{r}_n \cdot \mathbf{s}).$$

Following Eq. (9.5) the beam of an array with  $M$  sensors for a seismic signal with the specific slowness  $s_o$  is defined as

$$b(t) = \frac{1}{M} \sum_{j=1}^M w_j(t + \mathbf{r}_j \cdot \mathbf{s}_o) = w(t). \quad (9.11)$$

The seismic signal at sensor  $A_n$  of a plane wave for any other slowness  $s$  can be written as  $w_n(t) = w(t - \mathbf{r}_n \cdot \mathbf{s})$  and the beam is given by

$$b(t) = \frac{1}{M} \sum_{j=1}^M w_j(t + \mathbf{r}_j \cdot \mathbf{s}). \quad (9.12)$$

If we calculate all time shifts for a signal with the (correct) slowness  $s_o$  (Eq. (9.11)) with the (wrong) slowness  $s$  (Eq. (9.12)), we get the difference for the signal at site  $A_n$   $w(t + \mathbf{r}_n \cdot \mathbf{s}_o - \mathbf{r}_n \cdot \mathbf{s}) = w(t + \mathbf{r}_n \cdot (s_o - s))$  and the calculated beam can be written as

$$b(t) = \frac{1}{M} \sum_{j=1}^M w_j(t + \mathbf{r}_j \cdot (s_o - s)). \quad (9.13)$$

This beam is now a function of the difference between the two slowness values  $(s_o - s)$  and the geometry of the array  $\mathbf{r}_j$ . If the correct slowness is used, the beam calculated with Eq. (9.13) will be identical to the original signal  $w(t)$ . The seismic energy of this beam can be calculated by integrating over the squared amplitudes:

$$E(t) = \int_{-\infty}^{\infty} b^2(t) dt = \int_{-\infty}^{\infty} \left[ \frac{1}{M} \sum_{j=1}^M w_j(t + \mathbf{r}_j \cdot (s_o - s)) \right]^2 dt. \quad (9.14)$$

This equation can be written in the frequency domain by using Parzeval's theorem and the shifting theorem:

$$E(\omega, s_o - s) = \frac{1}{2\pi} \int_{-\infty}^{\infty} |\bar{w}(\omega)|^2 \cdot \left| \frac{1}{M} \sum_{j=1}^M e^{i\omega \mathbf{r}_j \cdot (s_o - s)} \right|^2 d\omega \quad (9.15)$$

with  $\bar{w}(\omega)$  being the Fourier transform of the seismogram  $w(t)$ . Using the definition of the wavenumber vector  $\mathbf{k} = \omega \cdot \mathbf{s}$ , we can also write  $\mathbf{k}_o = \omega \cdot \mathbf{s}_o$ :

$$E(\omega, \mathbf{k}_o - \mathbf{k}) = \frac{1}{2\pi} \int_{-\infty}^{\infty} |\bar{w}(\omega)|^2 \cdot |C(\mathbf{k}_o - \mathbf{k})|^2 d\omega, \text{ where}$$

(9.16)

$$|C(\mathbf{k}_o - \mathbf{k})|^2 = \left| \frac{1}{M} \sum_{j=1}^M e^{i\omega \mathbf{r}_n \cdot (\mathbf{k}_o - \mathbf{k})} \right|^2$$

(9.17)

Eq. (9.15) or Eq. (9.16) defines the energy of an array beam for a plane wave with the slowness  $s_o$  but calculating the applied time shifts for a slowness  $s$ . If the difference between  $s_o$  and  $s$  changes, the resulting beam has different amplitudes. However, this dependency is not a function of the actual signals observed at the single sites but a function of the array geometry weighted with the slowness difference  $\mathbf{r}_n \cdot (\mathbf{k}_o - \mathbf{k})$ . If the slowness difference is zero, the factor  $|C(\mathbf{k}_o - \mathbf{k})|^2$  becomes 1.0 and the array is optimally tuned for this slowness. All other energy propagating with a different slowness will be (partly) suppressed. Therefore Eq. (9.17) is called the transfer function of an array. This function is not only dependent on the slowness of the seismic phase observed with this array, but is also a function of the wavenumber  $k$  (i.e., wavelength or frequency) of the observed signal, and of the array geometry.

Some general rules about transfer characteristics of arrays can be formulated as follows:

- 1) The aperture of an array defines the resolution of the array for small wavenumbers. The larger the aperture is, the smaller the wavenumbers (or slownesses) is that can be measured with the array. The upper limit for the longest wavelength  $\lambda$  that can meaningfully be analyzed by array techniques is about the aperture  $a$  of the array. The array responds like a single station for signals with  $\lambda \gg a$ .
- 2) The number of sites controls the quality of the array as a wavenumber filter, i.e., its ability to suppress energy crossing the array at the same time with a different slowness.
- 3) The distances between the seismometers define the position of the side lobes in the array transfer function and the largest resolvable wavenumber: the smaller the mean distance, the smaller the wavelength of a resolvable seismic phase will be (for a given seismic velocity).
- 4) The geometry of the array defines the azimuth dependence of points 1 – 3.

Some of these points can be seen in the following two examples of array transfer functions. Fig. 9.21 shows the transfer function of the cross-shaped Yellowknife array (YKA). Fig. 9.22 shows as another example the array transfer function of the circular, small aperture array ARCES. The geometry of this array (see Fig. 9.1) gives a perfect azimuthal resolution, and side lobes of the transfer function are far away from the main lobe. However, because of the small aperture, this array can not distinguish between waves with small wavenumber differences, as can be seen in the relatively wide main lobe of the transfer function. In contrast, in the case of Yellowknife, the main lobe is very narrow because of the larger aperture of the array. This results in a higher resolution in measuring apparent velocities. But the array shows resolution differences in different azimuths, which are caused by its geometry. The many side lobes of the transfer function are the effect of the larger distances between the single array sites.

## 9. Seismic Arrays

Details on array design for the purpose of maximizing the gain achievable by beamforming can be found in 9.8.1.

In the next sections we will introduce “f-k analysis” and “beampacking” methods. In principle, it is all a matter of forming beams with different slowness vectors and comparing the amplitudes or the power of the beams, and then finding out which  $v_{app}$ -backazimuth combination gives the highest energy on the beam, i.e., to find out which beam is the “best” beam. In f-k analysis the process is done in the frequency domain rather than in the time domain.

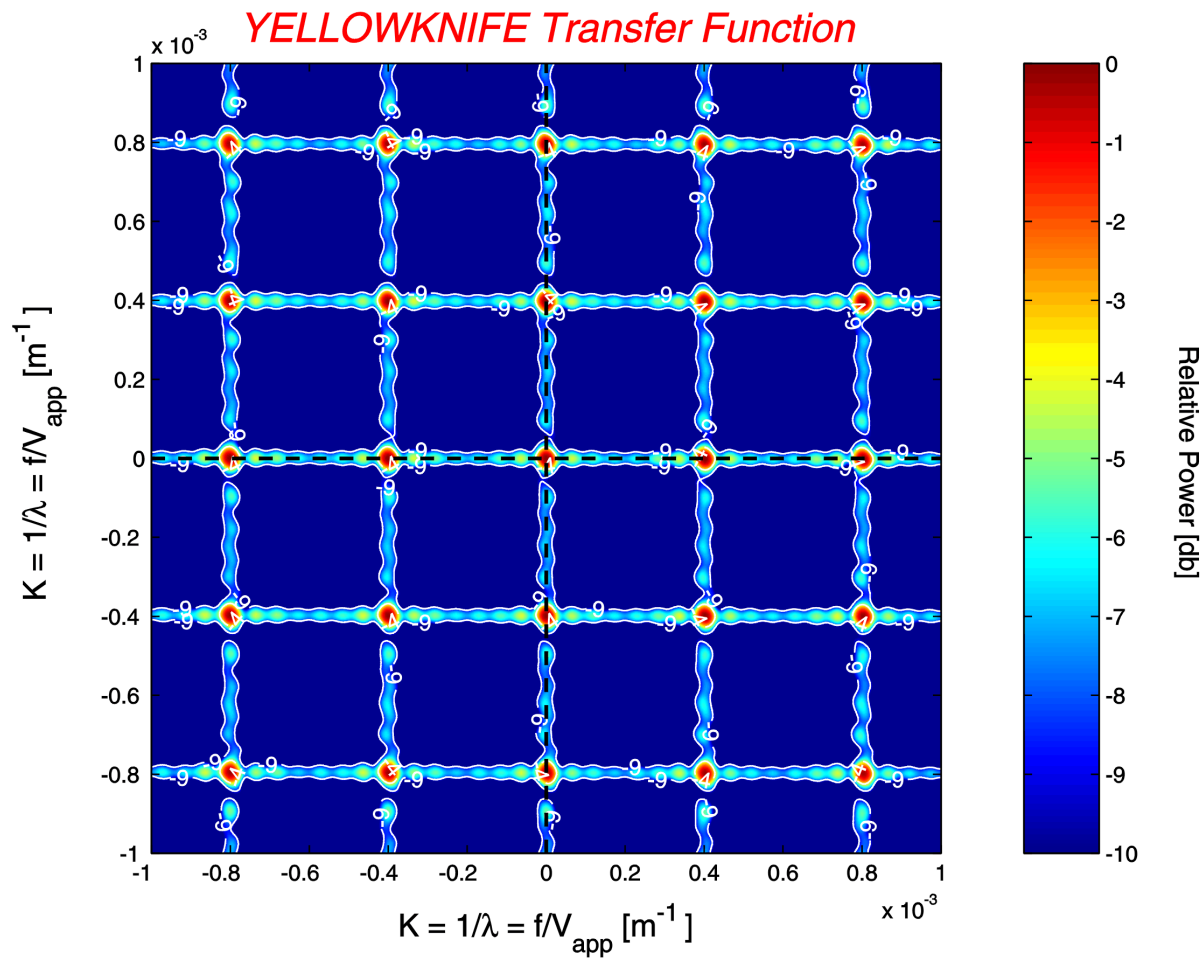


**Fig. 9.21** This figure shows the array transfer function of the cross-shaped Yellowknife array (see Fig. 9.3). Plotted is the relative power of the array response normalized with its maximum.

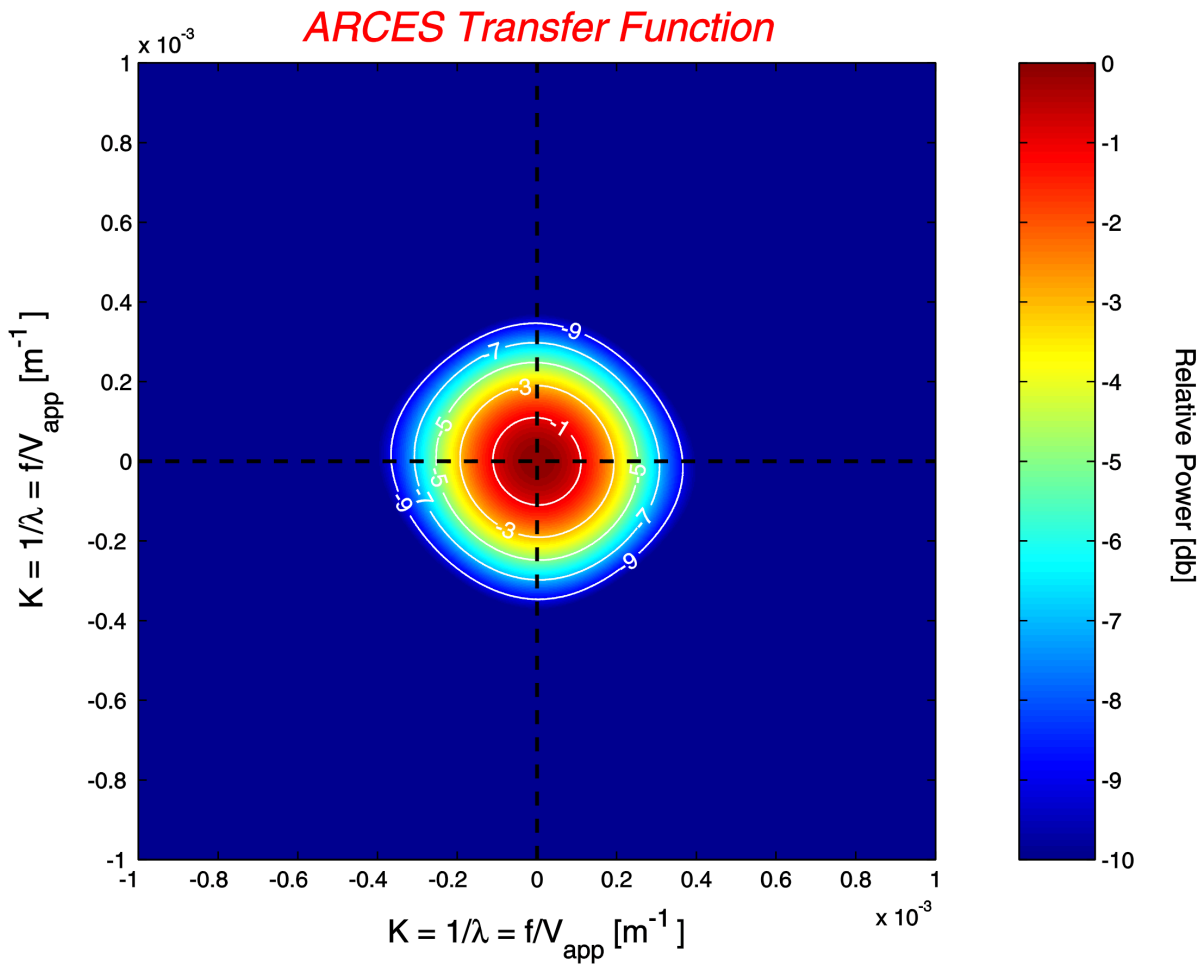


**Fig. 9.22** This figure illustrates the array transfer function of the circular ARCES array (see Fig. 9.1). Shown is the relative power of the array response normalized with its maximum. White isolines were plotted at -1, -3, -5, -7, and -9 db below the maximum of the array response.

## 9.7 Slowness estimation using seismic arrays

### 9.7.1 Slowness estimate by f-k analysis

A description of frequency-wavenumber analysis – “f-k analysis” – may be found in Capon (1969). This method has been further developed to include wide-band analysis, maximum-likelihood estimation techniques, and three-component data (Kværna and Doornbos, 1986; Kværna and Ringdal, 1986; Ødegaard et al., 1990).

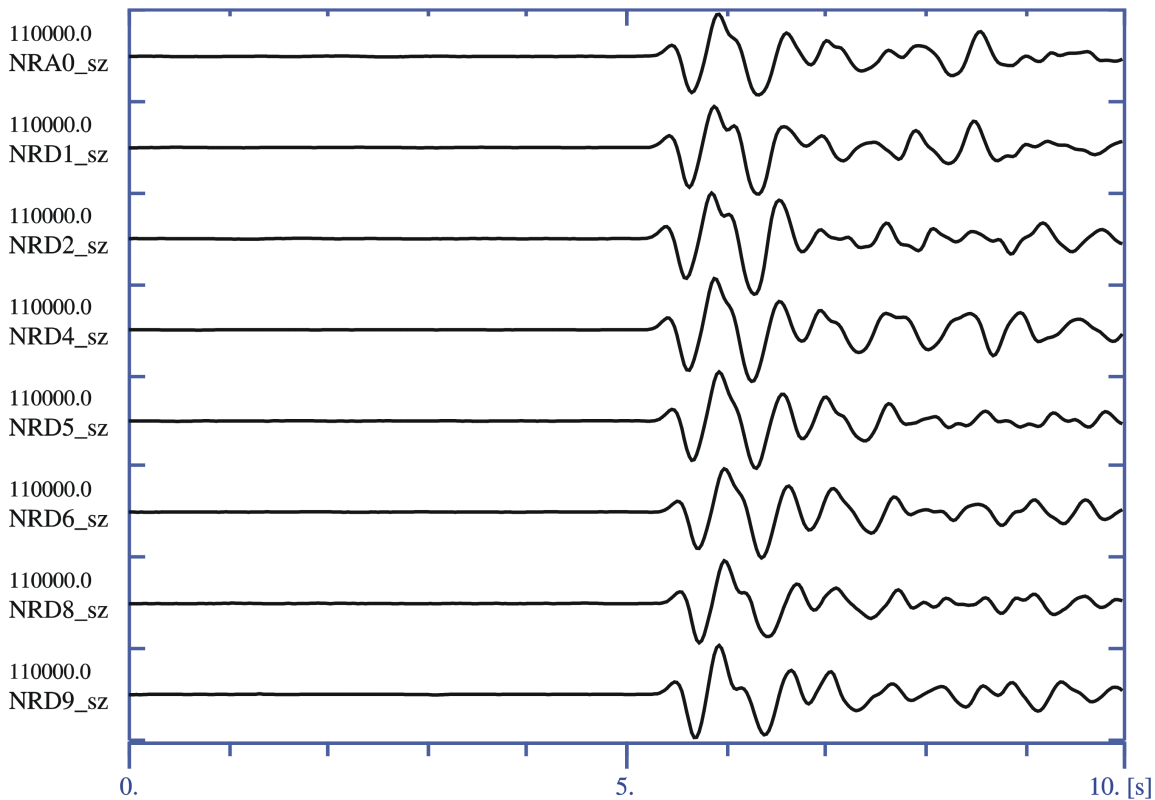
The f-k analysis is used as a reference tool for estimating slowness; f-k analysis is done in the frequency domain, and a time shift in the time domain is equivalent to a phase shift in the frequency domain. The principle is beamforming in the frequency domain for a number of different slowness values. Normally we use slownesses from -0.4 to 0.4 s/km equally spaced over 51 by 51 points. For every one of the 2601 points the beam power is evaluated, giving an equally spaced grid of 2601 power points.

## 9. Seismic Arrays

Such a power grid is displayed in Fig. 9.24 with the slowness ranging from -0.2 to 0.2 s/km; the unfiltered data used are shown in Fig. 9.23. The power is displayed by isolines of dB down from the maximum power. A process is used which will find the maximum power in the grid, and the corresponding slowness vector is the resulting estimated slowness.

The f-k plot in Fig. 9.24 also represents the color-coded relative power of the multichannel signal for 51 by 51 points in slowness space. Because the f-k analysis is a frequency-domain method, one has to define an interesting frequency range. In our case the data were analyzed in the frequency range between 1.2 and 3.2 Hz. The peak level is found at an apparent velocity 20.3 km/s, backazimuth 83.4°. The normalized relative peak power is 0.96. This measure tells us how coherent the signal is between the different sites and that a beam formed with the corresponding slowness will give a signal power that is 0.96 times the average power of the individual sensors. This means that the estimated beam signal will have practically no signal loss for this slowness and in this filter band as compared to individual sensors. The isolines tell us that using any different slowness will give a signal loss of maximum 10 dB. The equivalent beam total power is 84.22 dB.

An uncertainty of the estimated apparent velocity and backazimuth can be derived from the size of the observed power maximum in the f-k plot at a given db level below the maximum, the SNR of the signal, and the power difference between the maximum and an eventually existing secondary maximum in the plot.



1995-135:04.14.41.2 NORES

Lop Nor 1995-135:04.05.58.7 (origin time)

**Fig. 9.23** NORES recordings (raw data) of a Lop Nor explosion on May 15, 1995. Traces from the center site A0 and the D-ring instruments are shown at the same scale.

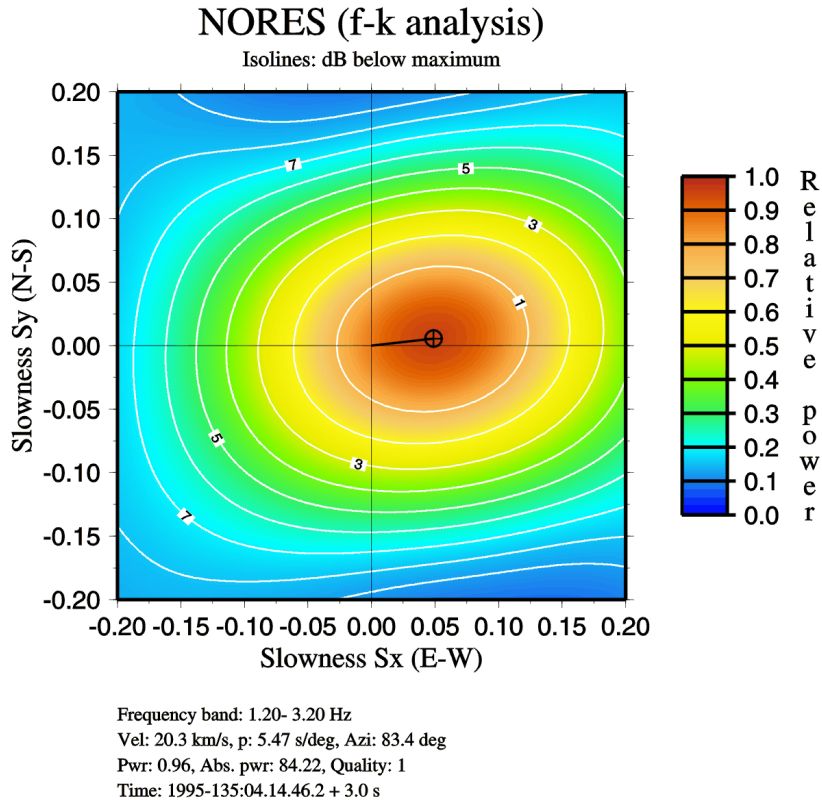


**Fig. 9.24** Result from wide-band f-k analysis of NORES data from a 3 second window around the signal shown in Fig. 9.23. The isolines are in dB from maximum peak and the color-coded relative power is a measure of signal coherence.

### 9.7.2 Beampacking (time domain wavenumber analysis)

An alternative to the technique described above is the beampacking scheme, i.e., to beamform over a predefined grid of slowness points and measure the power. As an example see Fig. 9.25, where we used the same NORES data as for the f-k analysis in Fig. 9.24. All data were prefiltered with a Butterworth 1.2 – 3.2 Hz bandpass filter to make the results comparable with the f-k result in Fig. 9.24. To obtain a similar resolution as for the f-k analysis, the time domain wavenumber analysis requires a relatively high sample rate of the data. Therefore, we oversampled the data in this example 5 times by interpolation, i.e., we changed the sample rate from 40 to 200 Hz.

One can see from the beamforming process that we get practically the same slowness estimate as for the f-k analysis in the frequency domain (Fig. 9.24). In the time domain case, the relative power is the signal power of the beam for the peak slowness divided by the average sensor power in the same time window. The total power of 91.45 dB in Fig. 9.25 is the maximum beam power.

Compared to the f-k process used, the resulting total power is now 6 dB higher, which is due to the measurement method, and not a real gain. However, the beamforming process results in a slightly (about 10%) narrower peak for the maximum power as compared to f-k analysis.

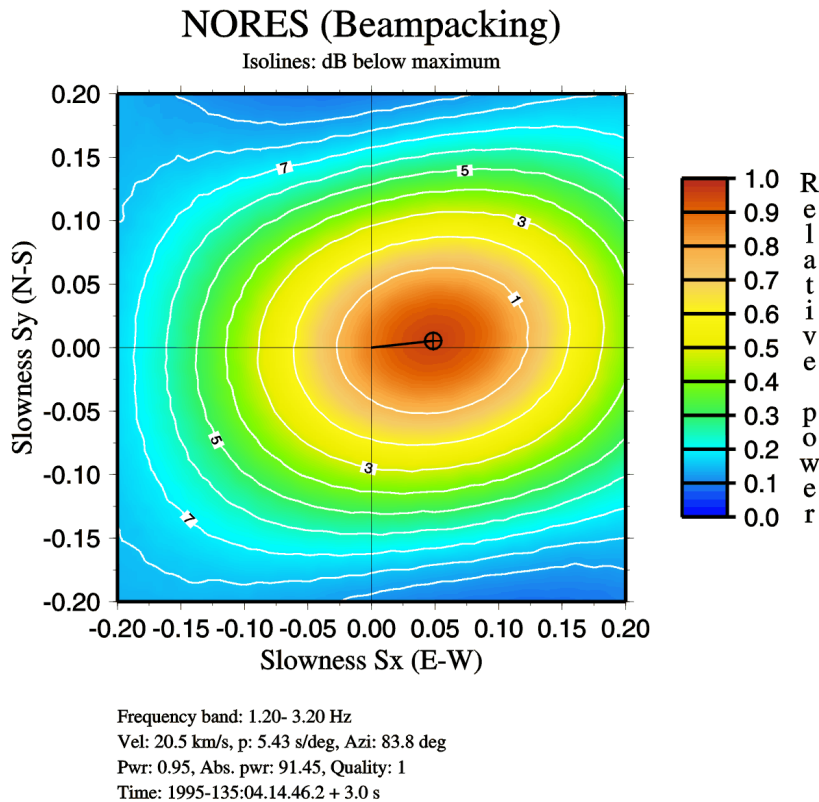


**Fig. 9.25** Result from beampacking of the NORES data in Fig. 9.24 in an equispaced slowness grid. The data were prefiltered in the band 1.2 – 3.2 Hz and were resampled to 200 Hz. The isolines represent power of each beam within the 3-second window analyzed.

### 9.7.3 Slowness estimate by time picks

Yet another way of estimating slowness is to carefully pick times of the first onset or any other common distinguishable part of the same phase (same cycle) for all instruments in an array. Assuming again that the wavefront is plane, we may use Eq. (9.18) to estimate the slowness vector  $s$  by least squares fit to the observations.

Let  $t_i$  be the arrival time picked at site  $i$ , and  $t_{ref}$  be the arrival time at the reference site, then  $\tau_i = t_i - t_{ref}$  is the observed time delay at site  $i$ . We observe the plane wave at  $M$  sites. With  $M \geq 3$ , we can estimate the horizontal components  $(s_x, s_y)$  of the slowness vector  $s$  by using least squares techniques. If  $M \geq 4$ , the vertical component of the slowness vector ( $s_z$ ) can also be resolved. The uncertainties of the estimated parameters can be calculated in parallel with solving the equation system of Eq. (9.18).

$$\sum_{i=1}^M (\tau_i - \mathbf{r}_i \cdot \mathbf{s})^2 = \min \quad (9.18)$$

This method requires interactive analyst work. However, to obtain automatic time picks and thereby provide a slowness estimate automatically, techniques like cross-correlation (matched filtering) or just picking of peak amplitude within a time window (for phases that have an impulsive onset and last two or three cycles) may be used.

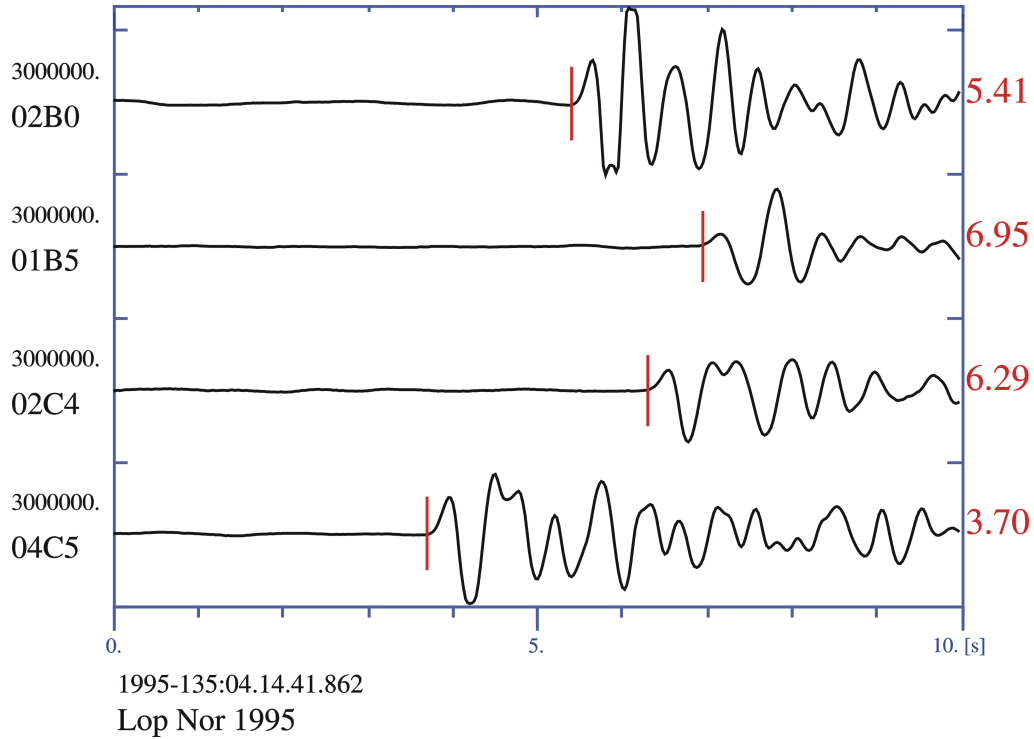


**Fig. 9.26** NORSAR recording of the Lop Nor explosion of May 15, 1995. Vertical traces (sz) from the sites 02B0, 01B5, 02C4, and 04C5 of the NORSAR array (see also Fig. 9.2) are shown at the same amplitude scale. Note the large time delays as compared to the smaller NORES array in Fig. 9.23. The figure illustrates a simple time pick procedure of the individual onsets. A plane wave fit to these 4 onset time measurements gives an apparent velocity of 16.3 km/s and a backazimuth of 77.5°.

#### 9.7.4 Time delay corrections

Calculating time delays using  $\tau_i = \mathbf{r}_i \cdot \mathbf{s}$  is a simplification, ignoring both elevation of instruments and the fact that seismic waves are not plane waves over an array of diameter of e.g., 60 km. We have to introduce a correction  $\Delta\tau_i$ . The deviation from plane-wave time delays is caused by instrument elevation differences and inhomogeneities in the Earth.

Including elevation when calculating time delays as done in section 9.4.4 may compensate for the deviation due to elevation differences. Historically, and for convenience, elevation corrections have not been used for NORSAR array beamforming. Instead, time delays have been calculated as plane-wave time delays plus a correction:

$$\tau_i = \mathbf{r}_i \cdot \mathbf{s} + \Delta\tau_i. \quad (9.19)$$

A database with time delay corrections was established that corrected for both elevation differences and inhomogeneities, and this database is still in use (Berteussen, 1974). So, for all beamforming, including each point in the beampacking process, the delays are corrected according to Eq. (9.19). The corrections depend on  $\mathbf{s}$ .

A method to determine velocity heterogeneities by inverting such deviations of observed onset times from the theoretical plane wave was developed at NORSAR, the so-called ACH method (Aki, Christofferson, and Husebye, 1977).

### 9.7.5 Slowness corrections

When observing the backazimuth of an approaching wave, we find deviations from the expected backazimuth. In addition, the observed ray parameter will also be different from the theoretical one. This observation is valid for any seismic station. If the deviation is systematic and consistent for a given source location (or small region), we can correct for this deviation. If the predicted slowness is  $s_c$  and the observed slowness is  $s_o$  (Fig. 9.27), then the slowness deviation is

$$\Delta s = s_o - s_c . \quad (9.20)$$

It is also common to use the ray parameter  $p$  [ $\text{s}/^\circ$ ] and the backazimuth BAZ [ $^\circ$ ] as slowness vector components and to express the residuals as:

$$\Delta p = p_o - p_c \text{ and } \Delta \text{BAZ} = \text{BAZ}_o - \text{BAZ}_c . \quad (9.21)$$

However, every array has to be calibrated with its own corrections. Numerous studies have been performed to obtain slowness corrections for different seismic arrays (see e.g., Berteussen, 1976 and for the reference lists in Krüger and Weber, 1992 or in Schweitzer, 2001b). Usually the derivation of slowness corrections for the whole slowness range observable with one array needs a large amount of corresponding data and therefore some time.

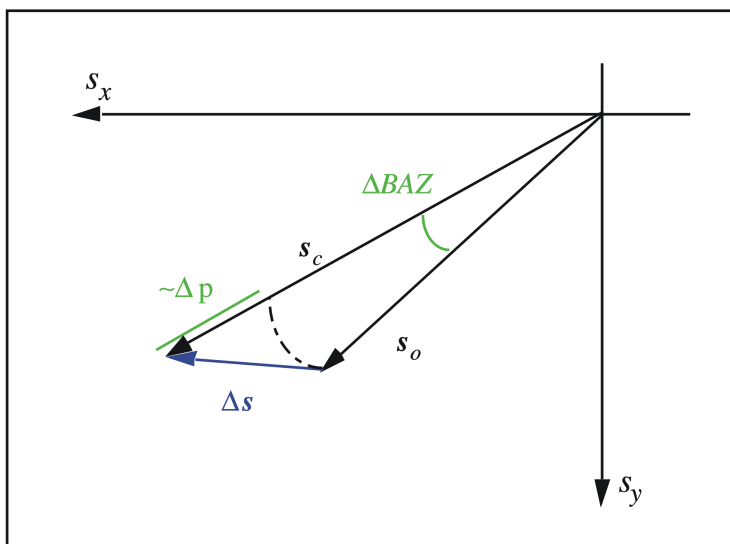


**Fig. 9.27** Slowness vector deviation in the horizontal plane. The vector  $s_c$  denotes theoretical slowness. The vector  $s_o$  denotes observed slowness. The vector  $\Delta s$  denotes the slowness residual, also referred to as mislocation vector. The length of the slowness vector measured in [ $\text{s}/^\circ$ ] is the ray parameter  $p$ , and the angle between North and the slowness vector, measured clockwise, is the backazimuth BAZ.

### 9.7.6 The correlation method used at the UKAEA arrays

As discussed in 9.6, the array transfer function of the UKAEA array YKA shows strong side lobes along a rectangular grid (see Fig. 9.21). This effect can be observed at all orthogonal linear or L-shaped arrays (Birtill and Whiteway, 1965). To improve the lower resolution along these principal axes, a correlation method has been introduced. In a first step, theoretical beams are separately calculated for each of the two seismometer lines; the geometrical crossing point of the two linear subarrays is used as the common reference point for both beams. If the actual signal has the same slowness as the slowness used to calculate the two beams, the signal must be in phase on both beams. In a second step calculating the cross-correlation between the two beams tests this condition. The correlator trace is calculated for a short, moving time window. This non-linear process is very sensitive to small phase differences and improves the resolution of such arrays especially along the principal axes of their transfer functions (for further details see Whiteway, 1965; Birtill and Whiteway, 1965; Weichert et al., 1967).

### 9.7.7 The VESPA process

A method to separate signals propagating with different apparent velocities is the VElocity SPectrum Analysis (VESPA) process. The principal idea of this method is to estimate the seismic energy reaching an array with different slownesses and to plot the beam energy along the time axis. The usual way to display a vespagram is to calculate the observed energy for specific beams and to construct an isoline plot of the observed energy for the different slowness values. The original VESPA process was defined for plotting the observed energy from a specific azimuth for different apparent velocities versus time (Davies et al., 1971). Fig. 9.28 shows as an example the vespagram for a mine blast in the Khibiny Massif (Kola Peninsula) observed with the ARCES array. The underground blasting of about 190 tons of explosives occurred on December 21, 1992 at 07:10 (latitude  $67.67^\circ$ , longitude  $33.73^\circ$ ) at about  $3.55^\circ$  epicentral distance from ARCES. All beams were calculated with the theoretical backazimuth of  $118^\circ$ , and the seismograms were bandpass filtered between 2 and 8 Hz. Fig. 9.28 shows two of the filtered seismograms used to calculate the vespagram. The energy for the different slowness values was calculated for 3 seconds-long sliding windows moved forward in 0.5 s steps. The observed energy was normalized with the maximum value and the isolines were plotted as contour lines in [db] below this maximum. Note that the first two P onsets both have a slowness of about 0.125 s/km equivalent to an apparent velocity of 8 km/s: Pn and a superposition of onsets from several crustal phases. The S phases are clearly separated from the P phases in slowness; Sn with a slowness of about 0.225 s/km (apparent velocity of about 4.44 km/s) and the dominating Lg phase with a slowness of about 0.28 s/km or an apparent velocity of about 3.57 km/s.

## 9. Seismic Arrays

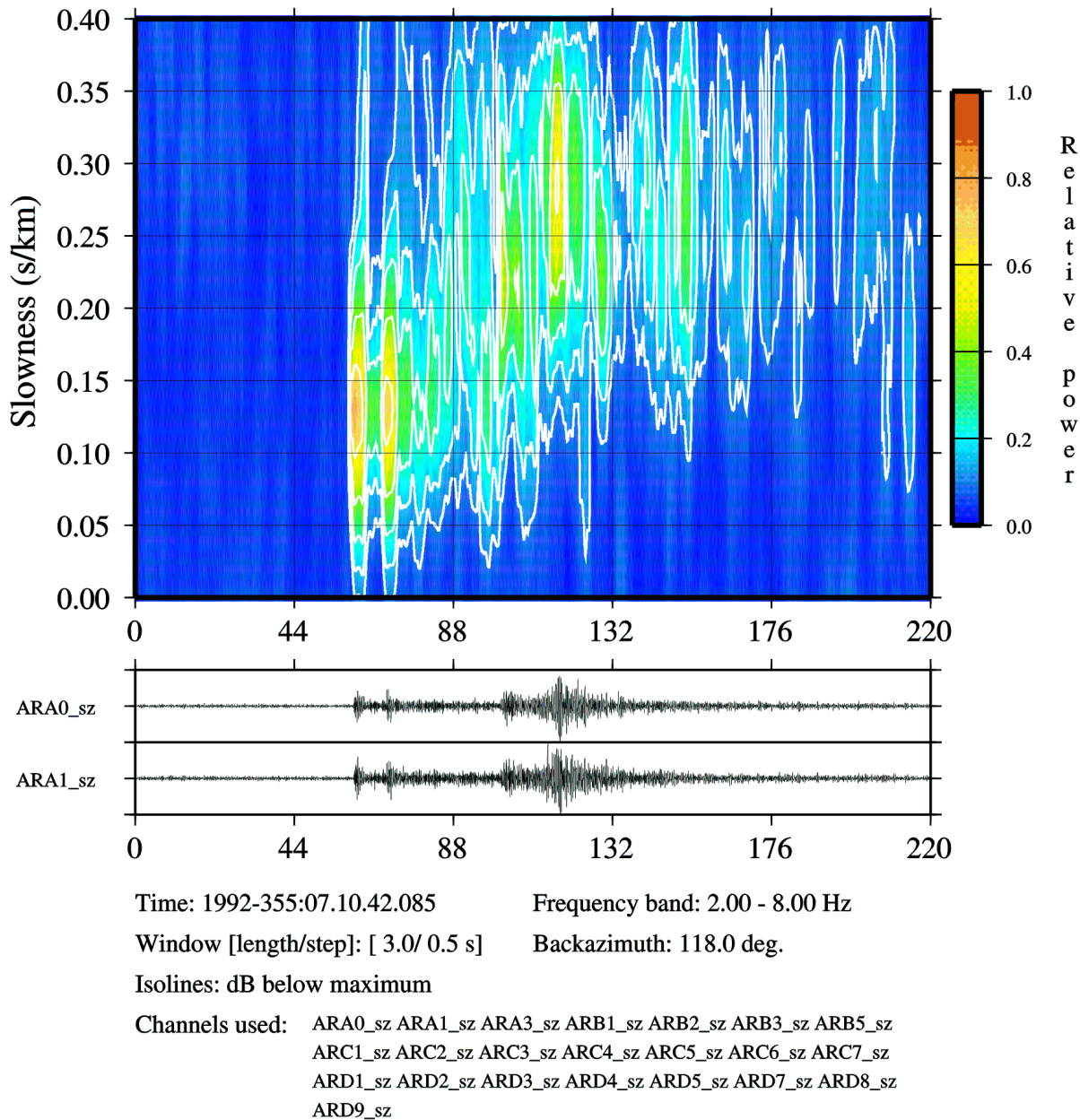


**Fig. 9.28** Vespragram for a mining explosion (December 21, 1992; 07:10; lat.  $67.67^\circ$ , lon.  $33.73^\circ$ ) in the Khibiny Massif observed at ARCES. Shown is the observed seismic energy for different apparent velocities (slownesses) and a constant backazimuth of  $118^\circ$ . For further details see text.

Later the concept vespragram was expanded by plotting the observed energy from different azimuths using a specific apparent velocity. Fig. 9.29 shows an example for such a plot for the same event in the Khibiny Massif as for Fig. 9.28. Instead of a constant backazimuth, a constant apparent velocity of 8 km/s was used to calculate the beam energy from all azimuth directions. Note also that the noise contains energy with apparent velocities around 8 km/s, but this noise approaches the array from a different backazimuth ( $310^\circ$ ), and the crustal P phases show a slight shift in the backazimuth direction relative to the first mantle P phase (Pn).

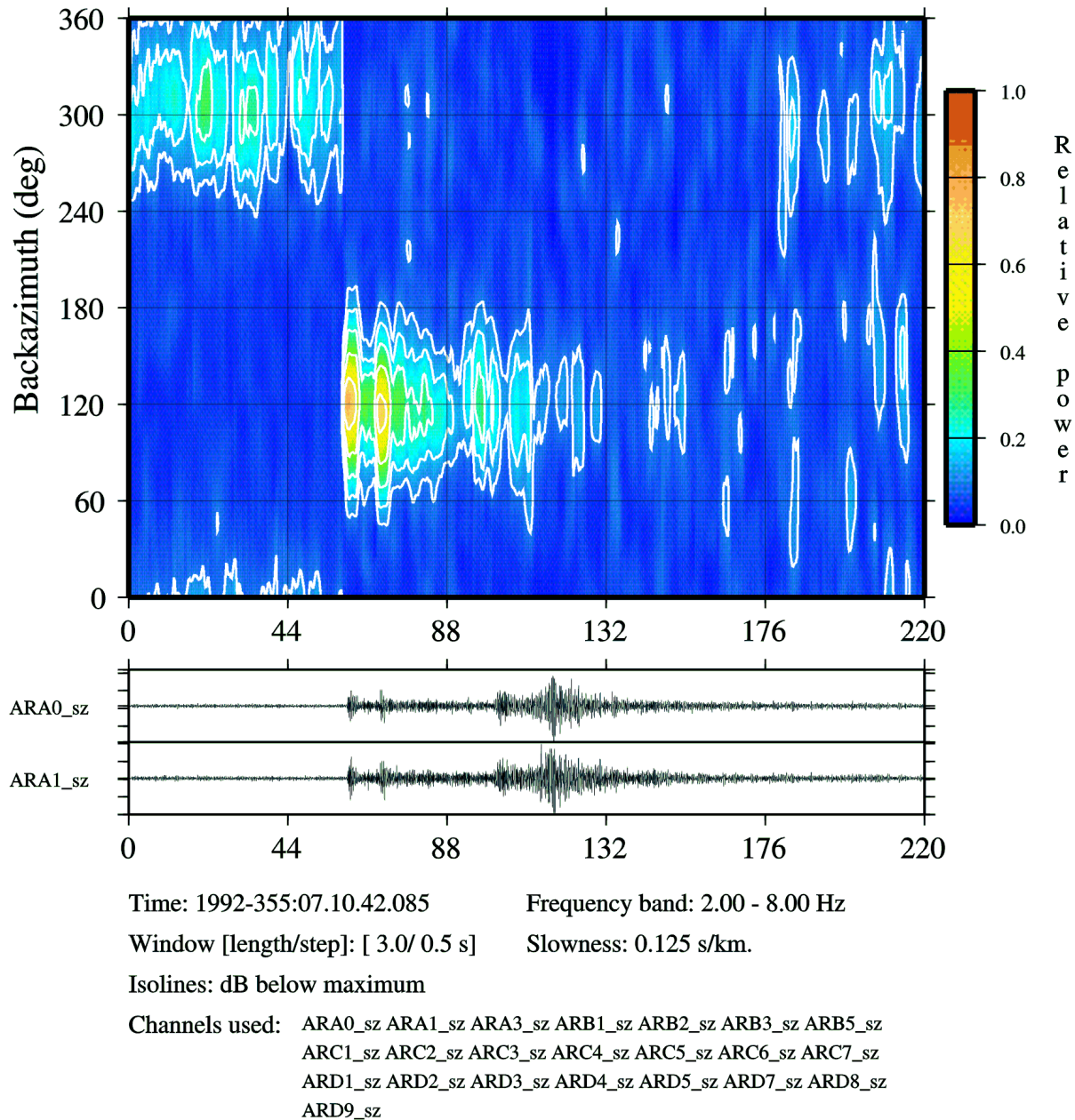


**Fig. 9.29** As Fig. 9.28 but the energy is now calculated for a constant apparent velocity of 8 km/s (i.e., a slowness of 0.125 s/km) and different backazimuths.

### 9.7.8 The n-th root process and weighted stack methods

A non-linear method to enhance the SNR during the beamforming is the so-called n-th root process (Muirhead, 1968; Kanasewich et al., 1973; Muirhead and Datt, 1976). Before summing up the single seismic traces, the n-th root is calculated for each trace by retaining the sign information; Eq. (9.5) then becomes:

$$B_N(t) = \frac{1}{M} \sum_{j=1}^M \left| w_j(t + \tau_j) \right|^{1/N} \cdot \text{signum}\{w_j(t)\}, \quad (9.22)$$

## 9. Seismic Arrays

where the value of the function  $signum\{w_j(t)\}$  is defined as -1 or +1, depending on the sign of the actual sample  $w_j(t)$ . After this summation, the beam has to be raised to the power of  $N$ , again retaining the sign information:

$$b_N(t) = |B_N(t)|^N \cdot signum\{B_N(t)\} \quad (9.23)$$

$N$  is an integer ( $N = 2, 3, 4, \dots$ ) that has to be chosen by the analyst. The  $n$ -th root process weights the coherence of a signal higher than the amplitudes, which results in a distortion of the waveforms: the larger  $N$ , the less the original waveform of the signal is preserved. However, the suppression of uncorrelated noise is better than with linear beamforming.

Schimmel and Paulssen (1997) introduced another non-linear stacking technique to enhance signals through reduction of incoherent noise, which shows a smaller waveform distortion than the  $n$ -th root process. In their method, the linear beam is weighted with the mean value of the so-called instantaneous phase of the actual signal. The phase term itself follows a power law, which can be defined by the analyst. With this phase-weighted stack all phase-incoherent signals will be suppressed and small coherent signals will be relatively enhanced.

Instead of the instantaneous phase, Kennett (2000) proposed the usage of the semblance of the signal as weighting function. He applied this approach not only on one (vertical) component of the observed wave field but also jointly on all three components. For this, he could also take into account the cross-semblance between the three components of ground movement. He achieved a similar resolution to the method of Schimmel and Paulssen (1997).

An easy implementable weighted stack method would be to weight the amplitudes of the single sites of an array with the SNR of the signal at this site before beamforming, but this does not directly exploit the coherence of the signals across the array. All described stacking methods can increase the slowness resolution of vespagrams (see 9.7.7).

## 9.8 Array design for the purpose of maximizing the SNR gain

Signal detection at array stations is governed by the gain that can be achieved in the signal-to-noise ratio (SNR) through the process of beamforming. This subsection provides some guidance as to how an array can be designed to maximize this gain. Other aspects of array design have been dealt with elsewhere in this chapter.

### 9.8.1 The gain formula

The SNR gain  $G$  by beamforming achievable from seismic array data can be expressed by

$$G^2 = \frac{\sum_{ij} C_{ij}}{\sum_{ij} \rho_{ij}} \quad (9.24)$$

## 9.8 Array design for the purpose of maximizing the SNR gain

where  $C_{ij}$  is the signal cross-correlation between sensors  $i$  and  $j$  of an array and  $\rho_{ij}$  is the noise cross-correlation between sensors  $i$  and  $j$  (see 9.4.5). For an  $N$ -sensor array, this formula collapses to the well-known relation of  $G^2 = N$  for perfectly correlating signals ( $C_{ij} = 1$  for all  $i$  and  $j$ ) and uncorrelated noise ( $\rho_{ij} = 0$  for  $i \neq j$  and  $\rho_{ii} = 1$  for  $i = j$ ).

For any array geometry it is thus possible to predict the array gain if the signal and noise cross-correlations are known for all pairs of sensors of the array layout. The remainder of this subsection describes how to design an array based on the availability of such correlation data.

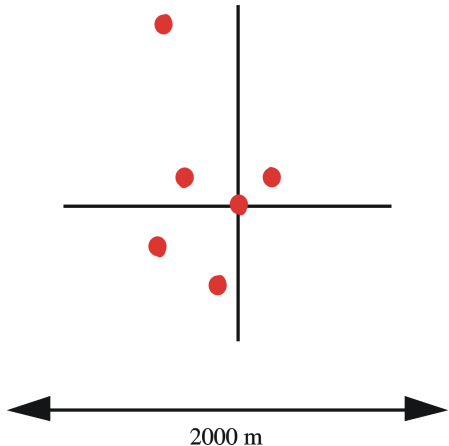


**Fig. 9.30** The figure shows the first layout for the experiments eventually leading to the 25-element NORES array in Norway in 1984.

### 9.8.2 Collection of correlation data during site surveys

Correlation data for use in the design phase should be collected in a carefully planned site survey. The sensor layout during the survey should be planned so to represent as many intersensor distances as possible. The first layout for the experiments eventually leading to the deployment in 1984 of the 25-element NORES array in Norway utilized only 6 sensors, in a rather irregular geometry, as shown in Fig. 9.30.

The deployment for the collection of the correlation data should be done in as simple a way as possible and should take advantage of outcropping bedrock where possible. The layout should preferably comprise ten sensors or more. If, however, for example only six sensors are available for the site survey, one could start out with a configuration something like that of Fig. 9.30 and record data continuously for about one week. At the end of this one-week period, one could redeploy four of the sensors and record data for another week. Two of the sensors would then occupy the same locations for the entire two-week recording period and would provide evidence (or lack thereof) of consistency in the results between the two one-week periods. The largest intersensor separation represented in these data should be, if possible, of the order of 3 km.

The experience from the design of the NORES array showed that the signal and noise correlation curves obtained from the early experiments (with six, and later twelve sensors) possessed most of the characteristic features and thus qualitatively resembled the curves derived later on from configurations comprising many more sensors (up to 25).

### 9.8.3 Correlation curves derived from experimental data

In the processing of the data from the site survey, cross-correlation values must be computed for all combinations of sensor pairs of the experimental layout. Consider, for example, a geometry of six sensors. This geometry comprises 15 unique pairs of sensors. Consider also a short interval of say 30 seconds of noise data (make sure no signal is contained in this time window) and compute the cross-correlation values for each of the 15 unique pairs of sensors (no time shifts are to be introduced for this computation). The time series are first bandpass filtered so as to derive the correlation values of one particular frequency (or frequency band). The 15 correlation values are then plotted in an x-y diagram, where the x-axis represents the intersensor separation and the y-axis the correlation value (a figure between -1.0 and +1.0), resulting in a plot as shown in Fig. 9.31.

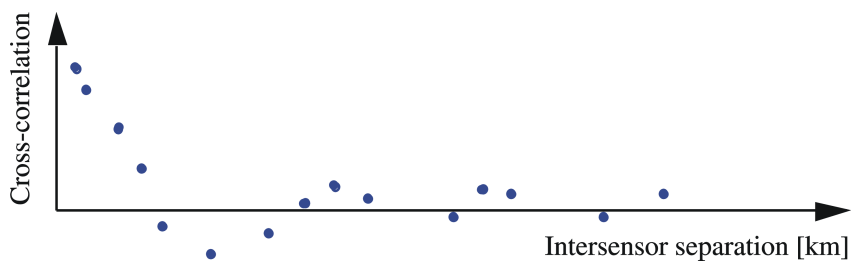


**Fig. 9.31** Noise cross-correlation values for a test layout of 6 sensors.

When plotting the cross-correlation values as a function of sensor separation only and thus disregarding possible directional dependencies, an implicit assumption is made of azimuthal symmetry in wavenumber space, over a longer time interval. This assumption is justified by the NORES experience, which shows that only a relatively small scatter is exhibited in the correlation data.

Computations of the kind described above should also be done for signals, which for the purpose of this section will be assumed to be P waves (although design strategies for the detection of S-type phases will be similar to those described here). A recording period of 14 days or so during the site survey hopefully should be sufficient to record a reasonable number of representative P-wave arrivals. The time windows for these computations should be relatively short (5 seconds or so) to capture the coherent part of the signal arrival. Signal time series must be aligned in accordance with the signal slowness (phase velocity and direction of approach) before the cross-correlation is computed. Again, the time series must be filtered in a relatively narrow band around the peak frequency of the signal being considered. A plot like the one shown in Fig. 9.32 would result from this, again assuming a six-sensor layout with 15 unique combinations of sensor pairs.

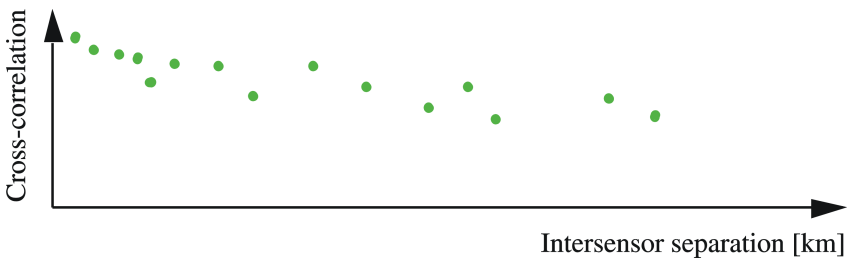


**Fig. 9.32** P-wave cross-correlation values for a test layout of 6 sensors.

Computations as described above should be repeated for various time intervals for the noise, and for various P arrivals recorded during the site survey. Then, for each frequency interval of interest, all data (both noise and signal correlation data) should be combined in one diagram for the purpose of deriving curves (based on interpolation) that are representative of that frequency interval, and that would provide correlation values for all intersensor separations. These diagrams might then appear as shown in Fig. 9.33, in which the upper curve represents the signal correlation and the lower curve the noise correlation.

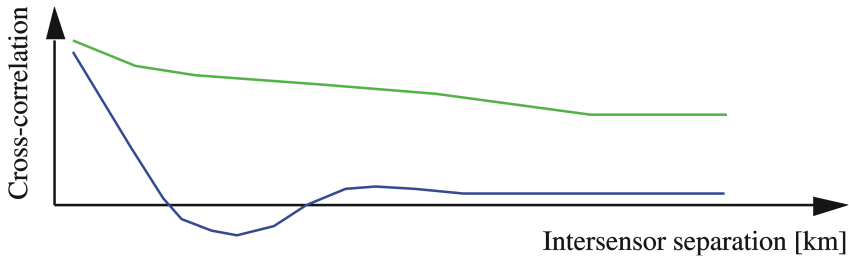


**Fig. 9.33** Signal (upper) and noise (lower) correlation curves representing experimental data collected for a test array.

For the noise correlation curve in Fig. 9.33 to be representative for 2 Hz, for example, the noise data should be filtered in a band where 2 Hz is close to the lower limit of the passband, due to the spectral fall-off of the noise. A passband of 1.8 – 2.8 Hz might be appropriate for the noise, but actual noise spectra for the site in question should be computed and studied before this passband is decided on. To generate a signal correlation curve representative for 2 Hz, signals should be used that have their spectral peaks close to this frequency, and some narrow passbands centered on 2 Hz should be applied to the data. These curves would then be used to predict gains for various array designs as detailed below.

It should be noted that the rather pronounced negative minima for the noise correlation curves (as schematically represented in Fig. 9.33) are consistently observed for the NORES array. It is the exploitation of this feature that provides for gains in excess of  $\sqrt{N}$ , commonly observed at the NORES array (or subgeometries thereof). It should also be noted that this feature of negative noise correlation values is not a universal one; e.g., Harjes (1990) did not find consistently such pronounced negative minima for the GERES test array in Germany.

#### **9.8.4 Example: A possible design strategy for a 9-element array**

As an example of application of the design ideas outlined above, let us consider practical aspects of the design of a 9-element array. Several new arrays to be built for the International Monitoring System (IMS) for CTBT monitoring will comprise 9 elements. A useful design for a new 9-element array would be one for which there are 3 and 5 elements equidistantly placed on each of two concentric rings, respectively, plus one element at the center of the geometry, as shown in Fig. 9.34.

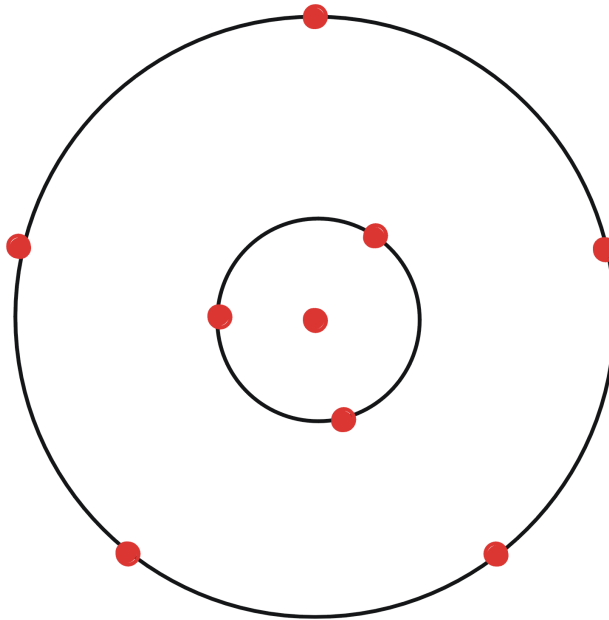


**Fig. 9.34** The figure shows a possible design for a 9-element array.

The elements on the two rings should be placed so as to avoid radial alignment. If the five elements of the outer ring are placed at 0, 72, 144, 216 and 288 degrees from due north, the elements of the inner ring might be placed at 36, 156 and 276 degrees, as shown in Fig. 9.34. Within this class of design, the problem at hand is thus to find the radii of the two rings that for a given site would provide the best overall array gain. To constrain the design options even further, one might consider adopting the NORES design idea, limited to these two rings. The radii of the four NORES rings are given by the formula:

$$R = R_{\min} \cdot 2.15^n, (n = 0, 1, 2, 3) \quad (9.25)$$

For NORES,  $R_{\min} = 150$  m. For the design problem at hand, only  $R_{\min}$ , the radius of the inner ring, remains to be determined from the correlation data, whereas the radius of the outer ring would then be 2.15 times the radius of the inner ring.

The final step in the procedure outlined here is to compute expected gains for various array designs within this class of geometries. To this end, one must determine which signal frequencies are of the largest importance with regard to the detection capability of the array at the site under study. Assuming that three P-wave signal frequencies,  $f_1$ ,  $f_2$  and  $f_3$ , (e.g., 1.8, 2.5 and 3.5 Hz) have been identified, these should be taken into account in the computations to derive the optimum array geometry. We would then have available from the site survey empirically-based correlation curves in analytical or tabular form that would provide correlation values for **all** intersensor separations of interest. The gains as a function of frequency for various values of the parameter  $R_{\min}$  could then be computed using the formula for the array gain and the correlation values derived from the correlation curves, for the relevant intersensor separations. The results of these computations could be tabulated as indicated in Tab. 9.1.

**Tab. 9.1** The table provides the gains by beamforming achievable by different values of the parameter  $R_{min}$ .

$R_{min}$ [m]	Gain ( $f_1$ ) [dB]	Gain ( $f_2$ ) [dB]	Gain ( $f_3$ ) [dB]
200	3	6	8
300	4	8	9
400	5	9	7
...	...	...	...
1000	9	7	4
...	...	...	...

Note that for the lowest frequency considered ( $f_1$ ), it might pay in terms of array gain to exclude the elements of the inner ring from the gain computations (since noise correlation values for low frequencies may be high for many sensor pairs involving sensors of the inner ring).

The optimum geometry would correspond to the value of  $R_{min}$  that gives the best overall gain in Tab. 9.1. This judgment would be based on some appropriate weighting scheme for the frequencies considered.

The procedure outlined here could be generalized to a class of designs for which the radii of the two rings are varied independently. Gain values would then be tabulated as shown in Tab. 9.1, but there would now be a sequence of tables (each table would represent a fixed radius of one of the two rings). The search for the optimum geometry would then be performed across all these tables.

## 9.9 Routine processing of small-aperture array data at NORSAR

### 9.9.1 Introduction

By way of example we will explain now the main features of the automatic routine processing of data from the regional arrays at NORSAR (Fyen 1989, 2001).

The array processing is divided into three steps:

- Detection Processing (DP), i.e., perform STA/LTA triggering on a number of predefined beams;
- Signal Attribute Processing (SAP), i.e., perform signal feature extraction of detected signals; and
- Event Processing (EP), i.e., perform phase association, location processing and event plotting.

We have earlier pointed out the importance of beamforming and filtering for signal enhancement. Fig. 9.35 shows ARCES data with one of the seismometer outputs filtered in different filter bands. An important feature seen from this figure is that the regional seismic phases Pn and Lg have their best SNR in different frequency bands. So to be sure to detect both phases, we should use several filter bands in the detector recipe. Fig. 9.18 showed

## 9. Seismic Arrays

different beams for the same P-wave signal. The other important lesson is that we need beams for various slowness vectors to detect the signal. In Mykkeltveit et al. (1988) and in Kværna (1989), it is shown that different combinations of sensors, for example, within the NORES array give different noise reduction for various frequency bands. The lesson is that it is not always optimal to use all seismometers of the array to form a beam; rather one should in general use different sub-configurations, tailored to the signal frequencies.

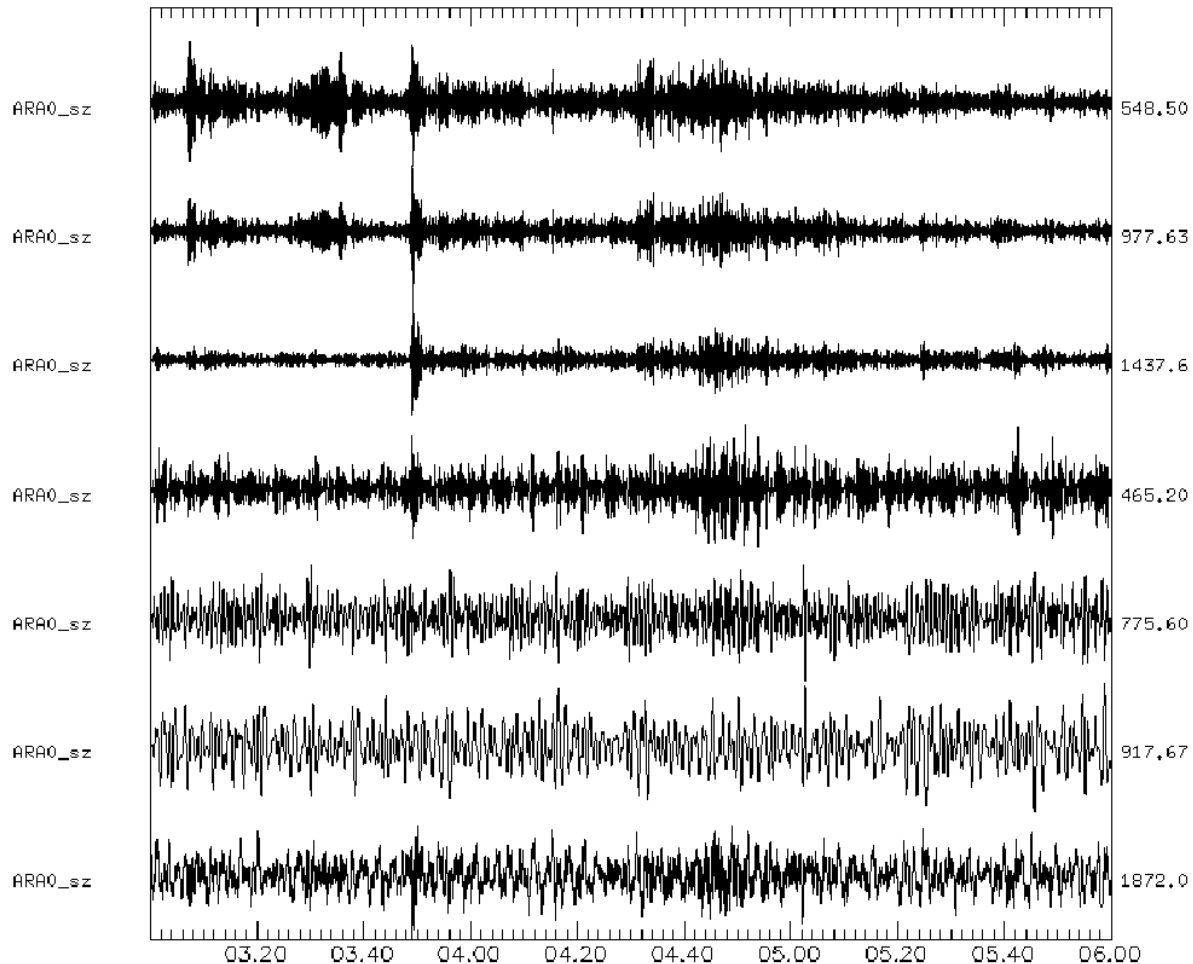


**Fig. 9.35** The bottom trace of the figure shows raw data from instrument A0 at the center of the ARCES array. The next traces from bottom to top are data from the same instrument filtered with 3rd order Butterworth bandpass filters using frequency bands 0.5 – 1.5 Hz, 1.0 – 3.0 Hz, 2.0 – 4.0 Hz, 4.0 – 8.0 Hz, 6.0 – 12.0 Hz, and 8.0 – 16.0 Hz, respectively.

Now we have three parameter sets that make up the input for the STA/LTA detector: the specific array configuration to use for the beam, the slowness vector to use for the beam, and the filter band to use for the beam. Note that one could also use just a single seismometer instead of a beam. Based on experiments, a list of these parameters has been compiled at NORSAR that constitute a “detector recipe” with, e.g., numerous beams using different slownesses, different configurations, and different filter bands. For a large signal, the detector

## 9.9 Routine processing of small-aperture array data at NORSAR

program will trigger on many beams, and the program will use a detection reduction process to report only one detection for each signal.

As an example, a detector recipe listing the entire beam set composed of 254 beams for the online processing of data from the SPITS array, as it is in use at NORSAR, is included in Tab. 9.2. The complete process is illustrated by using a data example from the ARCES array.

**Tab. 9.2** The detection beamset for the SPITS array as used at NORSAR. THR is the SNR threshold used to define a detection and “all” means that the whole SPITS array (SPA0, SPA1, SPA2, SPB1, SPB2, SPB3, SPB4, and SPB5) is used to form this beam (from Schweitzer, 1998).

BEAM NAMES	VELOCITY [km/s]	BACKAZIMUTH [deg]	FILTER		THR	SITES (verticals only)
			bandpass [Hz]	order		
S001	99999.9	0.0	0.8 – 2.0	4	4.5	SPA0 SPB1 SPB2 SPB3 SPB4 SPB5
S002	99999.9	0.0	0.8 – 2.0	4	4.5	all
S003	99999.9	0.0	1.0 – 3.0	3	4.5	SPA0 SPB1 SPB2 SPB3 SPB4 SPB5
S004	99999.9	0.0	1.0 – 3.0	3	4.5	all
S005	99999.9	0.0	2.0 – 4.0	3	4.0	SPA0 SPB1 SPB2 SPB3 SPB4 SPB5
S006	99999.9	0.0	2.0 – 4.0	3	4.0	all
S007	99999.9	0.0	3.0 – 5.0	3	4.0	SPA0 SPB1 SPB2 SPB3 SPB4 SPB5
S008	99999.9	0.0	3.0 – 5.0	3	4.0	all
S009	99999.9	0.0	0.9 – 3.5	4	4.5	SPA0 SPB1 SPB2 SPB3 SPB4 SPB5
S010	99999.9	0.0	0.9 – 3.5	4	4.5	all
S011	99999.9	0.0	1.0 – 4.0	3	4.5	SPA0 SPB1 SPB2 SPB3 SPB4 SPB5
S012	99999.9	0.0	1.0 – 4.0	3	4.5	all
SA01 – SA04	10.0	0 90 180 270	1.0 – 3.0	3	4.5	SPA0 SPB1 SPB2 SPB3 SPB4 SPB5
SA05 – SA08	10.0	45 135 225 315	1.0 – 3.0	3	4.5	all
SA09 – SA12	10.0	0 90 180 270	2.5 – 4.5	3	4.0	SPA0 SPB1 SPB2 SPB3 SPB4 SPB5
SA13 – SA16	10.0	45 135 225 315	2.5 – 4.5	3	4.0	all
SA17 – SA20	10.0	0 90 180 270	4.0 – 8.0	3	4.0	SPA0 SPB1 SPB2 SPB3 SPB4 SPB5
SA21 – SA24	10.0	45 135 225 315	4.0 – 8.0	3	4.0	all
SA25 – SA28	10.0	0 90 180 270	3.0 – 6.0	3	4.0	SPA0 SPB1 SPB2 SPB3 SPB4 SPB5
SA29 – SA32	10.0	45 135 225 315	3.0 – 6.0	3	4.0	all
SB01 – SB04	7.0	0 90 180 270	1.0 – 4.0	3	4.5	SPA0 SPB1 SPB2 SPB3 SPB4 SPB5
SB05 – SB08	7.0	45 135 225 315	1.0 – 4.0	3	4.5	all
SB09 – SB12	7.0	0 90 180 270	3.0 – 6.0	3	4.0	SPA0 SPB1 SPB2 SPB3 SPB4 SPB5
SB13 – SB16	7.0	45 135 225 315	3.0 – 6.0	3	4.0	all
SB17 – SB20	7.0	0 90 180 270	5.0 – 10.0	3	4.0	SPA0 SPB1 SPB2 SPB3 SPB4 SPB5
SB21 – SB24	7.0	45 135 225 315	5.0 – 10.0	3	4.0	all
SC01 – SC04	5.0	0 90 180 270	1.0 – 4.0	3	4.5	SPA0 SPB1 SPB2 SPB3 SPB4 SPB5
SC05 – SC08	5.0	45 135 225 315	1.0 – 4.0	3	4.5	all
SC09 – SC12	5.0	0 90 180 270	3.5 – 5.5	3	4.0	SPA0 SPB1 SPB2 SPB3 SPB4 SPB5
SC13 – SC16	5.0	45 135 225 315	3.5 – 5.5	3	4.0	all
SC17 – SC20	5.0	0 90 180 270	5.0 – 10.0	3	4.0	SPA0 SPB1 SPB2 SPB3 SPB4 SPB5
SC21 – SC24	5.0	45 135 225 315	5.0 – 10.0	3	4.0	all
SC25 – SC28	5.0	0 90 180 270	8.0 – 16.0	3	4.0	SPA0 SPB1 SPB2 SPB3 SPB4 SPB5
SC29 – SC32	5.0	45 135 225 315	8.0 – 16.0	3	4.0	all
SD01 – SD08	4.0	0 45 90 135 180 225 270 315	0.9 – 3.5	4	4.5	all
SD09 – SD16	4.0	0 45 90 135 180 225 270 315	3.0 – 6.0	3	4.0	all
SD17 – SD24	4.0	0 45 90 135 180 225 270 315	4.0 – 8.0	3	4.0	all
SE01 – SE08	3.3	0 45 90 135 180 225 270 315	1.5 – 3.5	3	4.5	all
SE09 – SE16	3.3	0 45 90 135 180 225 270 315	3.0 – 6.0	3	4.0	all
SE17 – SE24	3.3	0 45 90 135 180 225 270 315	5.0 – 10.0	3	4.0	all
SF01 – SF08	2.5	0 45 90 135 180 225 270 315	1.0 – 4.0	3	4.5	all
SF09 – SF16	2.5	0 45 90 135 180 225 270 315	2.0 – 4.0	3	4.0	all
SF17 – SF24	2.5	0 45 90 135 180 225 270 315	3.0 – 5.0	3	4.0	all
SN01	8.4	97.6	2.0 – 4.0	3	3.7	all
SN02	8.4	97.6	3.0 – 5.0	3	3.7	all
SN03	8.4	97.6	4.0 – 8.0	3	3.7	all
SN04	8.4	97.6	6.0 – 12.0	3	3.7	all
SN05	8.4	97.6	8.0 – 16.0	3	3.7	all
SN06	4.7	97.6	2.0 – 4.0	3	3.7	all
SN07	4.7	97.6	3.0 – 5.0	3	3.7	all
SN08	4.7	97.6	4.0 – 8.0	3	3.7	all
SN09	4.7	97.6	6.0 – 12.0	3	3.7	all
SN10	4.7	97.6	8.0 – 16.0	3	3.7	all
SG01 – SG12	2.0	0 30 60 90 120 150 180 210 240 270 300 330	1.5 – 3.5	3	4.5	all
SG13 – SG24	2.0	0 30 60 90 120 150 180 210 240 270 300 330	2.5 – 4.5	3	4.0	all
SG25 – SG36	2.0	0 30 60 90 120 150 180 210 240 270 300 330	3.5 – 5.5	3	4.0	all
SM01 – SM12	1.7	0 30 60 90 120 150 180 210 240 270 300 330	1.0 – 3.0	3	4.5	all
SM13 – SM24	1.7	0 30 60 90 120 150 180 210 240 270 300 330	2.0 – 4.0	3	4.0	all
SM25 – SM36	1.7	0 30 60 90 120 150 180 210 240 270 300 330	3.0 – 6.0	3	4.0	all

## 9. Seismic Arrays

### 9.9.2 Detection Processing – DP

The DP process continuously reads data off a disk loop or any other continuous database and uses beamforming, filtering, and the STA/LTA detector to obtain detections (triggers). The DP program produces, e.g., for the array ARCES (ARC) and for the day of the year (DOY) 199, 1996, the file ARC96199.DPX.

The following list gives some example lines from this file. The file contains the name of the detecting beam (e.g., F074), the time of detection (199:16.03.49.3), the end of the detection state (199:16.03.53.1), the maximum STA (242.4), the LTA at the time of detection (10.27), the SNR (STA/LTA = SNR = 23.601), and the number of beams detecting (37). The detecting beam reported (here F074) is the one beam, normally out of many beams, that detected this signal with the highest SNR.

FH04	199:16.02.18.6	-	02.19.9	106.52	32.15	3.313	1
FH04	199:16.02.39.1	-	02.39.6	116.09	43.91	2.644	1
FH04	199:16.02.44.4	-	02.48.6	296.52	56.63	5.236	5
F101	199:16.02.55.5	-	02.56.3	175.40	33.59	5.221	3
F074	199:16.03.49.3	-	03.53.1	242.40	10.27	23.601	37
FH03	199:16.04.32.9	-	04.35.9	291.46	73.01	3.992	5
FH02	199:16.04.46.4	-	04.50.9	297.87	75.23	3.960	24
FH04	199:16.09.57.6	-	09.58.9	80.86	24.07	3.359	2

The key parameters reported are the beam code, the trigger time, and the SNR = STA/LTA. The beam code points to a file (see Fig. 9.36) containing information on beam configuration, slowness and filter used. The format of a detection output is not important. The important thing is to create a list of detections that can be used for further analysis.

```
THR = 4.000
BF1 = 3.500
BF2 = 5.500
BMVEL = 11.100
BMAZI = 150.000
REFLAT = 69.535
REFLON = 25.506
REFELE = 403.000
REFSIT = ARA0_sz
SELECTED CHANNELS : ARA0_sz ARB1_sz ARB2_sz ARB3_sz ARB4_sz ARB5_sz
ARC1_sz ARC2_sz ARC3_sz ARC4_sz ARC5_sz ARC6_sz ARC7_sz
```

**Fig. 9.36** Example of the contents of a file with the parameters that characterize beam F074. THR is the SNR detection threshold, BF1 and BF2 are the lower and the upper limits of the bandpass filter applied, BMVEL and BMAZI are the apparent velocity and the backazimuth for this beam, REFLAT, REFLON, and REFSIT define the reference site of the beam, and SELECTED CHANNELS lists the site configuration.

### 9.9.3 Signal Attribute Processing – SAP

This process sequentially reads detections from the .DPX file and performs for every detection an f-k analysis to estimate apparent velocity and backazimuth. The estimated

velocity and backazimuth is referred to as “observed slowness”. Waveform segments for the analysis are again read from a disk loop or any other database.

A special version of the EP program is used and produces, e.g., for array ARC, DOY 199, 1996 the file ARC96199.FKX. The key parameters reported in the .FKX files are the signal onset time, the beam code, the SNR, the estimated slowness, the signal amplitude and frequency, and the phase identification based on the slowness estimate.

Some lines from ARC96199.FKX are listed below. The entries are the arrival id number (e.g., 25), the estimated onset time (199:16.03.48.409), the difference between trigger and onset time (0.89), the beam name (F074), the SNR (23.6), the apparent velocity from f-k analysis (7.4), the preliminary phase name by automatically considering apparent velocity and three-component polarization analysis (Pgn, which means either Pg or Pn), the estimated backazimuth from f-k analysis ( $122.5^\circ$ ), the relative power from f-k analysis (0.72, a number between 0.0 (no coherence) and 1.0 (perfect coherence, correlation)), the f-k analysis quality indicator (2, 1=best, 4=poor), the estimated dominant frequency in Hz (4.85), the maximum amplitude in counts (476.9), the maximum STA of the detection (242.4), the polarization analysis IP, IS (0 and -3, respectively), the polarization analysis rectilinearity (0.69), the horizontal/vertical ratio (0.49), the inclination 1 ( $41.26^\circ$ ), and the polarization inclination 3 ( $73.94^\circ$ ).

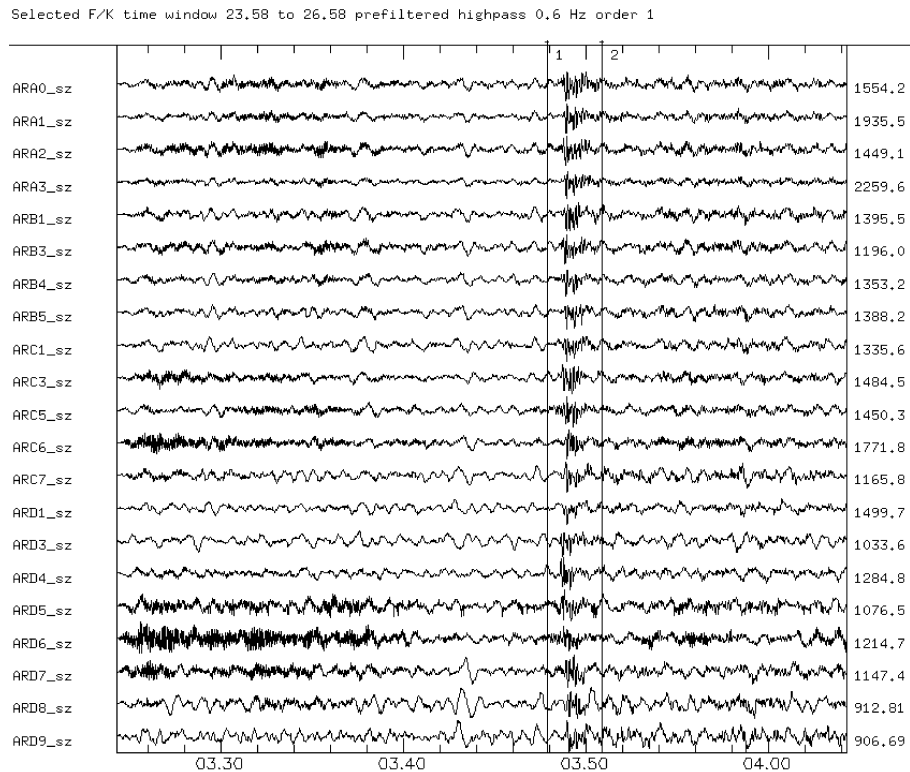
5	199:16.02.18.314	0.29	FH04	3.3	2.4	nois	256.5	0.33	4	9.22	336.2	106.5	1	-3	0.77	0.68	22.88	83.77
10	199:16.02.36.964	2.14	FH04	2.6	2.4	nois	247.8	0.38	3	9.93	439.5	116.1	1	-3	0.79	0.25	4.92	83.30
15	199:16.02.43.039	1.36	FH04	5.2	2.4	nois	243.3	0.59	3	9.80	931.2	296.5	1	-3	0.56	0.49	14.66	88.32
20	199:16.02.54.915	0.58	F101	5.2	2.4	nois	236.7	0.61	3	9.85	1019.8	175.4	0	0	-1.00	-1.00	-1.00	-1.00
25	199:16.03.48.409	0.89	F074	23.6	7.4	Pgn	122.5	0.72	2	4.85	476.9	242.4	0	-3	0.69	0.49	41.26	73.94
30	199:16.04.32.160	0.74	FH03	4.0	5.4	Lg	117.7	0.32	3	6.38	596.6	291.5	D4_sz	0.57	1.07	61.00	74.64	
35	199:16.04.45.785	0.61	FH02	4.0	4.1	Lg	127.4	0.27	3	5.07	531.9	297.3	D4_sz	0.48	1.36	58.36	54.76	
40	199:16.09.55.770	1.83	FH04	3.4	2.4	nois	197.7	0.44	4	9.33	227.5	80.9	-1	-2	0.70	1.23	85.50	72.81
45	199:16.10.38.771	1.73	F106	4.8	2.5	nois	222.0	0.52	3	8.38	230.4	59.7	0	2	0.88	2.38	81.32	28.00

Fig. 9.37 shows raw data for the detection reported at time 199:16.03.49.3 (see detection list). The signal attribute process will use this detection time to select a 3 second wide time window starting 0.5 second before the detection time. The data from all vertical seismometers within this time window will then be used for f-k analysis to obtain the true apparent velocity of the signal. The result from the f-k analysis is shown in Fig. 9.38. This process is repeated for all detections and Fig. 9.39 shows the data interval selected for the Lg detection. The corresponding f-k analysis results are shown in Fig. 9.40. In automatic mode, of course, the EP program will not display any graphics. The figures are only produced for illustration purposes. However, the capability of displaying results graphically at any step of a process is essential to be able to develop optimum recipes and parameters. The EP program may output results into flat files or a database.

For a large array like NORSAR we can, on the basis of the phase identification and measured slowness, get a distance by screening a slowness table and thereby a location using distance and backazimuth. This is a relatively minor operation in terms of CPU power, so with every detection a corresponding location is provided in the case of NORSAR processing.

For the large array NORSAR, we may choose between beamform f-k analysis and the beampacking process. The benefit of using beampacking rather than frequency domain f-k analysis is that for every point in slowness space, we can use time delay corrections and obtain a calibrated slowness.

## 9. Seismic Arrays



**Fig. 9.37** The figure shows raw data from all the vertical seismometers of the ARCES array. The time interval contains the Pn phase of a regional event. The vertical bars define a 3 second time window that is used for the f-k analysis.

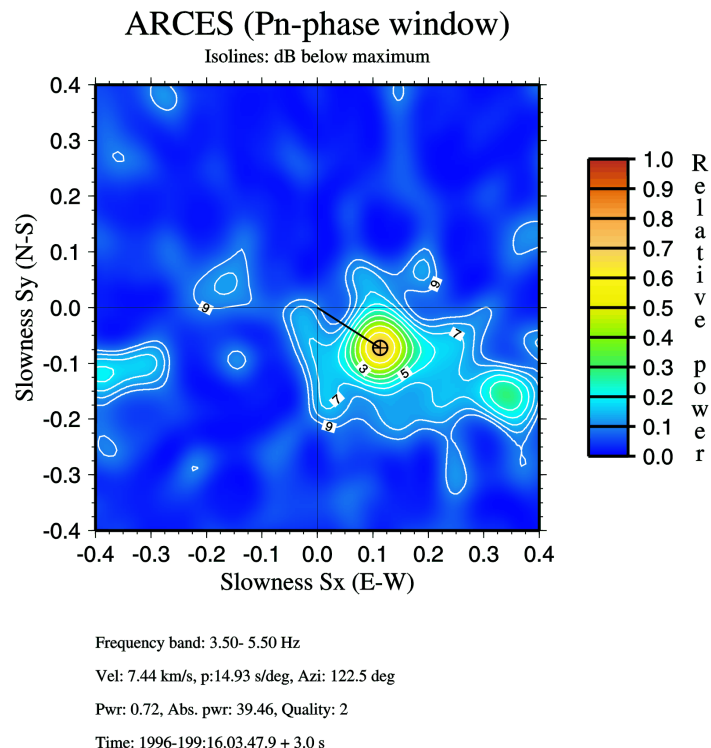


**Fig. 9.38** Result of the broadband f-k analysis from the data in Fig. 9.37, pertaining to the Pn-phase interval.

## 9.9 Routine processing of small-aperture array data at NORSAR

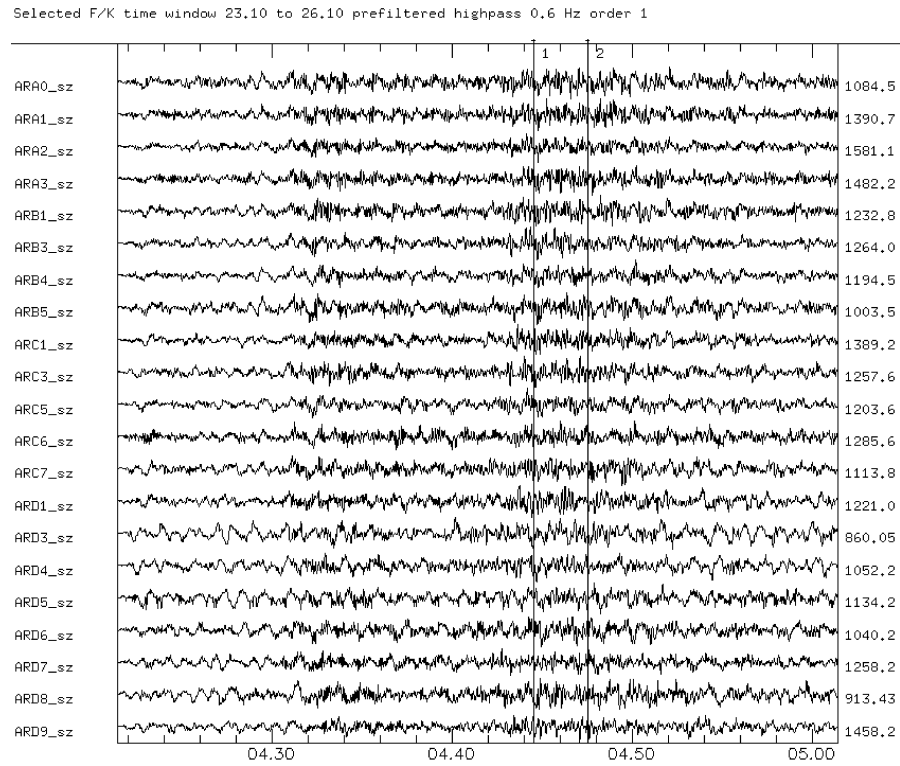


**Fig. 9.39** The figure shows raw data from all the vertical seismometers of the ARCES array. The time interval contains the Lg phase of a regional event. The vertical bars define a 3 second time window that is used for the f-k analysis.

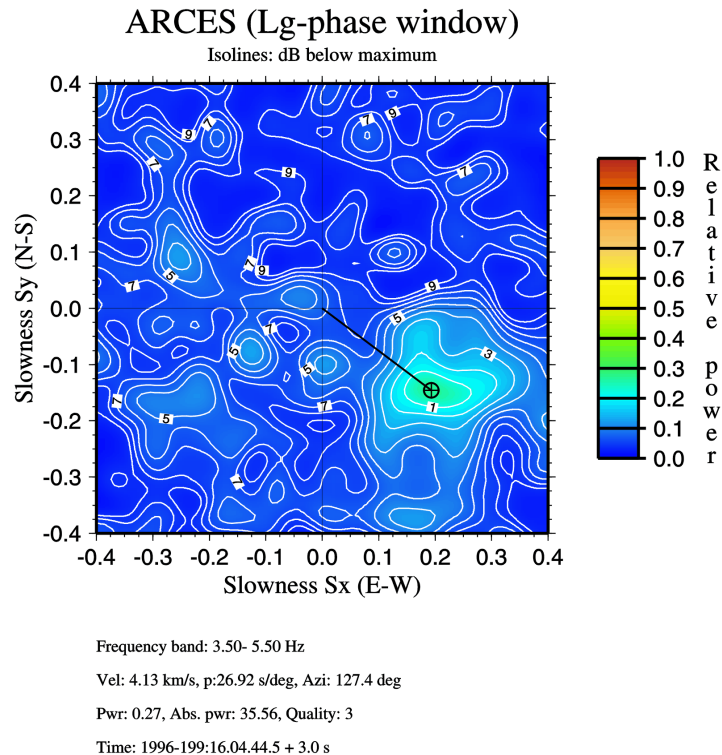


**Fig. 9.40** Result of the broadband f-k analysis from the data in Fig. 9.39, pertaining to the Lg-phase interval.

### 9.9.4 Event Processing – EP

This process sequentially reads all detections from the .FKX file. Whenever a detection with an apparent velocity greater than, e.g., 6.0 km/s is found, it is treated as P. Additional detections are searched for, and if additional detections are found with backazimuth estimates not more than, e.g.,  $30^\circ$  from the first detection and a detection time not more than 4 minutes from the first detection, they are used as associated detections. If detections with an apparent velocity less than 6.0 km/s are found, then they are treated as S (Sn, Lg). If phases within 4 minutes and backazimuth deviation of less than  $30^\circ$  with a first P and an S later are found, then they are treated as observations from a regional event. A location routine, which uses the backazimuth information, is used to locate the regional event. More details on these topics here are given in Mykkeltveit and Bungum (1984).

The result is written in the file ARC96199.EPX for array ARC, DOY 199, 1996. The key parameters reported are the origin time, the hypocenter, and the magnitude for each located event, and onset time, amplitude and frequency, SNR, beam code, and apparent velocity for all associated detections. For each declared event, an event plot may be created (see Fig. 9.41).

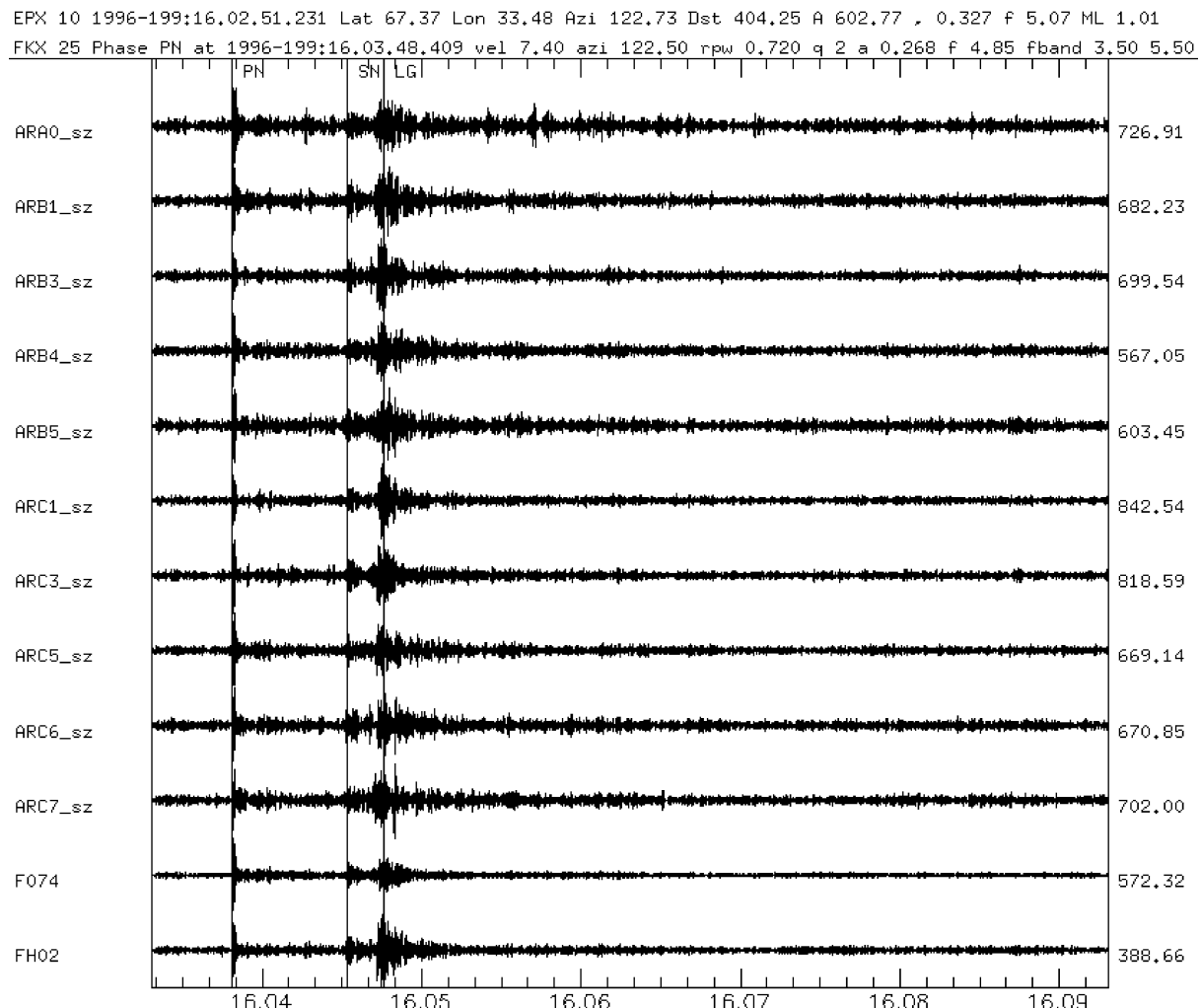


**Fig. 9.41** Regional event plot for final documentation.

Some lines from ARC96199.EPX are listed below. Whenever an event is declared, a location is performed and reported with two lines (HYP and EPX) that contain event number (10), origin time (199:16.02.51.2), latitude ( $67.369^\circ$ ), longitude ( $33.479^\circ$ ), ML (1.01), distance in [km] (404.3), backazimuth ( $122.7^\circ$ ), fixed depth (0F). The associated phases are listed thereafter, and for the Pn phase we have the id number (25), the arrival time (199:16.03.48.4), the station name (here FRS, the old NORSAR internal code for ARCES), the phase name (PN), the maximum amplitude in [nm] (0.268), the corresponding dominant frequency in [Hz] (4.8), the SNR (23.6), the beam name (F074), the apparent velocity (7.4), the backazimuth ( $122.5^\circ$ ), and an explanatory code from the location process. LOCATE means that this phase was used for location, ASSOC means that this onset was associated but not used in location, Tele means that this phase is interpreted as a teleseismic onset, Noplot3ci means that this phase was not used for any event definition. The “beam-name” aVG means that the corresponding arrival time is used for measuring the amplitude for ML, and the apparent velocity is the group velocity in that case.

5	199:16.02.18.3	FRS	nois	0.145	9.2	3.3	FH04	2.4	256.5	Noplot3ci
10	199:16.02.37.0	FRS	nois	0.194	9.9	2.6	FH04	2.4	247.8	Noplot3ci
15	199:16.02.43.0	FRS	nois	0.409	9.8	5.2	FH04	2.4	243.3	Noplot3ci
20	199:16.02.54.9	FRS	nois	0.448	9.9	5.2	F101	2.4	236.7	Noplot3ci
10	HYP 724 EUROPEAN USSR									
10	199:16.02.51.2	EPX		67.369	33.479	1.01		404.3	122.7	OF
25	199:16.03.48.4	FRS	PN	0.268	4.8	23.6	F074	7.4	122.5	LOCATE
30	199:16.04.32.2	FRS	SN	0.278	6.4	4.0	FH03	5.4	117.7	LOCATE
10	199:16.04.44.6	MAG	ML	0.327	5.1	602.8	aVG	3.6	122.7	LOCATE
35	199:16.04.45.8	FRS	LG	0.288	5.1	4.0	FH02	4.1	127.4	LOCATE

The above example identifies one group of phases with backazimuth around  $123^\circ$  that are within 4 minutes. The first phase within the group has regional P-wave apparent velocity, and it is followed by a phase with regional S apparent velocity. Those are the criteria for defining an event.

## **9.10 Operational or planned seismic arrays**

Tab. 9.3 below lists operational or planned seismic arrays as of September 2002. The following symbols have been used:

- ⊕ array, which is part of the International Monitoring System (IMS) to monitor the Comprehensive Nuclear-Test-Ban Treaty (CTBT) for nuclear tests as a primary or auxiliary station;
- \* circular array of NORES type design;
- \*\* array of UKAEA type design.

Free fields in Tab. 9.3 indicate that values are yet to be determined or are unknown to the authors of Chapter 9. Fig. 9.42 shows a map with all arrays listed in the table.

## 9. Seismic Arrays

**Tab. 9.3** List of operational or planned seismic arrays (as of September 2002)

CODE	LAT [°]	LON [°]	HEIGHT [km]	NUMBER OF ELEMENTS	APERTURE [km]	NAME
ABKT	37.9304	58.1189	0.678			Alibek ⊕
AKASG	50.4	29.1		26		Malin ⊕
ALAR	65.0653	-147.5639	0.626	6		Alaska Long-Period
APAES	67.6061	32.9931	0.200	9	1	Apatity *
ARCES	69.5349	25.5058	0.403	25	3	ARCESS ⊕ *
ASAR	-23.6664	133.9044	0.607	20	10	Alice Springs ⊕
BAO	-15.6349	-47.9915	1.211	12		Brasilia **
BCAR	63.0656	-141.785	0.847	5		Beaver Creek
BMAR	67.4289	-144.5807	0.756	5		Burnt Mountain
BMO	44.8489	-117.3056	1.189			Blue Mountains
BRLAR	39.7	33.6	1.4	8		Keskin Long-Period
BRSAR	39.7250	33.6389	1.440	7		Keskin ⊕
BRVK	53.0581	70.2828	0.315			Borovoye ⊕
CBAR	69.1266	-105.1120	0.040	23		Cambridge Bay
CM1	45.9337	-93.3527	0.324	6		Central Minnesota
CMAR	18.4575	98.9429	0.307	24	56	Chiang Mai ⊕
EKA	55.3317	-3.1592	0.263	20	9	Eskdalemuir ⊕ **
ESDC	39.6755	-3.9617	0.753	26	40	Sonseca ⊕
FINES	61.4436	26.0771	0.150	16	2	FINESS ⊕ *
FLAR	54.7188	-101.9958	0.229	19		Flin Flon
GBA	13.6042	77.4361	0.686			Gauribidanur **
GERES	48.8451	13.7016	1.132	25	4	GERESS ⊕ *
GRF	49.6900	11.2200	0.500	13	100	Gräfenberg
HFA0	60.1420	13.6850	0.275	10	1	Hagfors ⊕
HILR	49.5440	119.7450	0.6	9	4	Hailar ⊕
HLBN						Haleban
ILAR	64.7714	-146.8866	0.419	20		Eielson ⊕ *
IMAR	65.9835	-153.7491	0.372	5		Indian Mountain
IR1	35.4164	50.6888	1.347	7		Iran Long-Period
JAVM	48.0	106.8				Javhlant ⊕
KSAR	37.4211	127.8844	0.109	37		Wonju ⊕
KURK	50.7153	78.6203	0.184	21		Kurchatov ⊕
KVAR	43.9557	42.6952	1.196	4	0.3	Kislovodsk ⊕
LSU1	30.0733	-91.9821	-0.023	5	-0.023	Parcperdue
LUXOR	26.0	33.0				Luxor ⊕
LZDM	36.091	103.84	1.6	9	4	Lanzhou ⊕
MKAR	46.7937	82.2904	0.615	10	4	Makanchi ⊕
MJAR	36.5417	138.2088	0.422	7	10	Matsushiro ⊕
MMAI	33.0	35.4	0.4			Mount Meron (Parod) ⊕ *
NSD	65.1944	18.8185	.2	5	1	Näsudden (Malå)
NOA	61.0397	11.2148	0.717	42	60	NORSAR ⊕
NORES	60.7353	11.5414	0.302	25	3	NORESS *
NTA	37.2783	-116.4367	1.996			Nevada Test Site
NVAR	38.4296	-118.3036	2.042	14		Mina ⊕
PARI	33.65	73.252				Pari ⊕
PDAR	42.7667	-109.5579	2.214	14	4	Pinedale (Boulder) ⊕
PDYAR	59.6553	112.4408	0.489			Peleduy ⊕
PETKA	53.02	158.65	0.15			Petropavlovsk ⊕
PKF	35.8818	-120.4135	0.469			Parkfield
RC01	61.0894	-149.7367	0.374			Rabbit Creek

## 9.10 Operational or planned seismic arrays

SB1	31.21	-105.4378	1.570			Sierra Blanca
SONM	47.8083	106.4167				Songong
SPITS	78.1777	16.3700	0.323	9	1	Spitsbergen $\oplus$ *
TXAR	29.3338	-103.6670	1.013	9	4	Lajitas $\oplus$ *
USK	44.28	132.08	0.3			Ussuryisk $\oplus$
VNA2	-70.9252	-7.39267	0.350	16	2	Neumayer-Watzmann $\oplus$
WRA	-19.9426	134.3394	0.419	24	25	Warramunga $\oplus$ **
YKA	62.4932	-114.6053	0.197	20	25	Yellowknife $\oplus$ **
ZAL	53.94	84.80	0.2			Zalesovo $\oplus$
						(Niger) $\oplus$
						(Saudi Arabia) $\oplus$

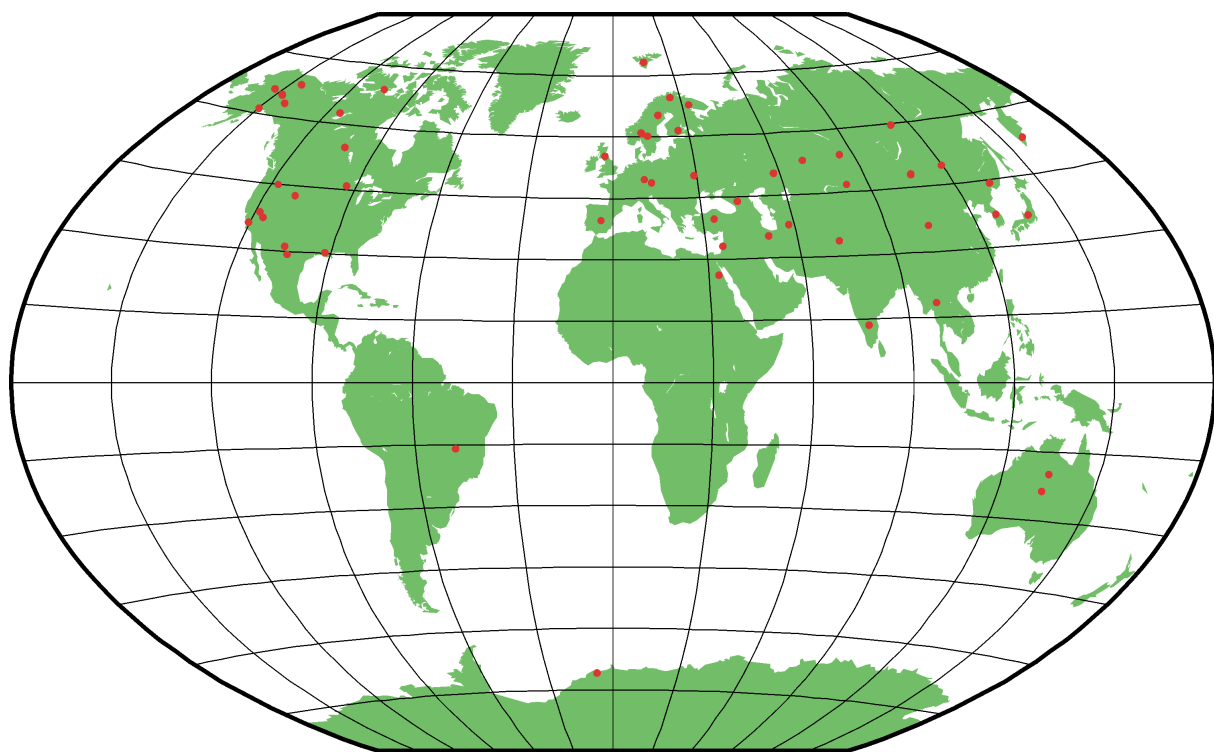


**Fig. 9.42** The map shows locations of operational and planned seismic arrays (as of September 2002).

## Acknowledgments

The authors thank John B. Young (Blacknest) for reprints of contributions from the old days of array seismology in Great Britain, and Peter Bormann, Brian Kennett, Frank Scherbaum, and Lyla Taylor for critical reviews of the manuscript. This is NORSAR contribution No. 685.

## **9. Seismic Arrays**